Deciphering the conditions of tochilinite and cronstedtite formation in CM chondrites from low temperature hydrothermal experiments

Lionel Vacher, Laurent Truche, François Faure, Laurent Tissandier, Régine Mosser-ruck, Yves Marrocchi

Deciphering the conditions of tochilinite and cronstedtite formation in CM chondrites from low temperature hydrothermal experiments

Lionel G. Vacher[a*], Laurent Truche[b], François Faure[a], Laurent Tissandier[a], Régine Mosser-Ruck[c] and Yves Marrocchi[a]

[a]CRPG, CNRS, Université de Lorraine, UMR 7358, Vandoeuvre-les-Nancy, F-54501, France
[b]ISTerre, UMR 5275 CNRS, Université Grenoble Alpes, 1381 rue de la Piscine, BP53 38041 Grenoble CEDEX 9, France
[c]GeoRessources, UMR 7359 CNRS, Université de Lorraine, Campus Aiguillettes, 54506 Vandoeuvre-lès-Nancy, France

[*]Corresponding author: lvacher@crpg.cnrs-nancy.fr

Keywords: CM chondrites, hydrothermal experiments, cronstedtite, tochilinite

Abstract—Tochilinite/cronstedtite intergrowths are commonly observed as alteration products in CM chondrite matrices but the conditions under which they formed are still largely under-constrained due to their scarcity in terrestrial environments. Here we report low temperature (80°C) anoxic hydrothermal experiments using starting assemblages similar to the constituents of the matrices of the most pristine CM chondrite and S-rich and S-free fluids. Cronstedtite crystals formed only in S-free experiments under circumneutral conditions with the highest Fe/Si ratios. Fe-rich tochilinite with chemical and structural characteristics similar to chondritic tochilinite was observed in S-bearing experiments. We observed a positive correlation between the Mg content in the hydroxide layer of synthetic tochilinite and temperature, suggesting that the composition of tochilinite is a proxy for the alteration temperature in CM chondrites. Using this relation, we estimate the mean precipitation temperatures of tochilinite to be 120-160°C for CM chondrites. Given the different temperature ranges of tochilinite and cronstedtite in our experiments, we propose that Fe-rich tochilinite crystals resulted from the alteration of metal beads under S-bearing alkaline conditions at T = 120-160°C followed by cronstedtite crystals in formed by reaction of matrix amorphous silicates, metal beads, and water at low temperature (50–120°C).

INTRODUCTION

C-type asteroids are the sources of undifferentiated carbonaceous meteorites and provide valuable information about the physicochemical conditions that prevailed in the solar protoplanetary disk. CM carbonaceous chondrites are fragments of these asteroids (Clark et al. 2010; Cloutis et al. 2011) and contain a significant amount of water (i.e., water/rock ratio = 0.4 upon accretion; Marrocchi et al. 2018), mainly as OH bound into phyllosilicates (Jarosewich 1990; Barber 1981). They are characterized by different degree of aqueous alteration, from moderately (CM2) to highly altered (CM1) (Zolensky et al. 1997; Rubin et al. 2007), and contain a variety of secondary phases produced through aqueous alteration processes, including carbonates, sulfides, oxides, and hydroxides (Bunch and Chang, 1980; Barber 1981; Tomeoka and Buseck, 1985; Zolensky et al. 1993; Brearley, 2006; Howard et al. 2009, 2011; Lee et al. 2014). The most characteristic secondary phases in CM chondrites are tochilinite-cronstedtite intergrowths (TCIs), occurring as complex assemblages dispersed throughout the chondrules, fine-grained rims and matrix (Fuchs et al. 1973; Tomeoka and Buseck 1985; Nakamura and Nakamuta 1996; Howard et al. 2015; Pignatelli et al. 2016, 2017). TCIs are ubiquitous in unheated CM chondrites and may be useful in deciphering the alteration conditions of CM parent bodies.

Since the first description of complex Fe-S-O alteration minerals in CM chondrites (i.e., as “poorly characterized phases”; Ramdohr 1963; Fuchs et al. 1973), numerous studies have sought to better understand the mineralogy and chemical properties of TCIs (Tomeoka and Buseck 1985; Mackinnon and Zolensky 1984; Zolensky and Mackinnon 1986; Nakamura and Nakamuta 1996; Palmer and Lauretta 2011; Pignatelli et al. 2016, 2017). Two types of TCIs have been defined based on morphology, mineralogy, and chemical composition (Nakamura and Nakamuta 1996): Type-I TCIs occur as rounded massive rims around Fe-Ni metal beads embedded in chondrules and comprise tochilinite with minor cronstedtite and goethite (Palmer and Lauretta 2011; Pignatelli et al. 2017), whereas Type-II TCIs occur as fibrous clusters in the matrix and comprise cronstedtite with minor tochilinite and magnetite (Pignatelli et al. 2017).

Tochilinite is a hydroxysulfide mineral with the general ideal formula of $2Fe_{1-x}S \cdot n(Fe,Mg,Al,Ca)(OH)_2$, where $0.08 \leq x \leq 0.28$ and $1.58 \leq n \leq 1.75$ (Zolensky and Mackinnon 1986; Gubaidulina et al. 2007). Its crystal structure is characterized by alternating brucite/amakinite-like $(Mg,Fe)(OH)_2$ and mackinawite-like $(Fe,Ni)_{1-x}S$ layers (Mackinnon and Zolensky 1984; Organova et al. 1988). Meteoritic tochilinite is believed to form during

the first stage of aqueous alteration by dissolution of Fe-Ni metal or olivine/pyroxene by S- and Fe-rich fluids (Zolensky and Mackinnon 1986; Palmer and Lauretta 2011; Pignatelli et al. 2016). Thermodynamic simulations and hydrothermal experiments indicate that tochilinite precipitates under very reducing conditions (log $fO_2 \approx -91$ to -85) in neutral-alkaline environments (pH = 7.8–14), typically at 80–320°C (Kakos et al. 1994; Browning and Bourcier 1996; Kozerenko et al. 1996; Moroz et al. 1997; Gubaidulina et al. 2007; Peng et al. 2007; Peng and Jing 2014). Cronstedtite is a Fe-rich phyllosilicate (7 Å along its *c*-axis) with the general formula $(Fe^{2+}_{3-x}Fe^{3+}_{x})(Si_{2-x}Fe^{3+}_{x})O_5(OH)_4$, where $0 \leq x \leq 0.84$ (Hybler et al. 2000; Kogure et al. 2002; Pignatelli et al. 2013): Fe^{3+} is in tetrahedral coordination, and cronstedtite forms a solid solution with greenalite $[(Fe^{2+}Fe^{3+})_3Si_2O_5(OH)_4]$ and chrysotile $[Mg_3Si_2O_5(OH)_4]$ in CM chondrites (Velbel 2014). Some Type-II TCIs display euhedral crystal faces suggesting that such TCIs result from the pseudomorphism of olivine, pyroxene, and carbonates (Browning and Bourcier 1996; Lee et al. 2013; Pignatelli et al. 2016; Vacher et al. 2017). Laboratory experiments and thermodynamic calculations suggest that cronstedtite forms under less reducing conditions than tochilinite (i.e., log $fO_2 \approx -75$ to -55) in neutral conditions (pH = 7–8) from Si- and Fe-rich fluids at 50–120°C (Lantenois et al. 2005; Lanson et al. 2012; Pignatelli et al. 2013, 2014; Zolotov 2014).

The occurrence of tochilinite and cronstedtite as intergrowths suggests that (i) these minerals may precipitated under similar physicochemical conditions at some point (Pignatelli et al. 2016, 2017) and/ or (ii) one could have replaced the other during the CM parent body evolution. Their stability fields remain poorly constrained, and few laboratory experiments have investigated the formation of tochilinite and cronstedtite from starting products similar to those encountered in CM chondrites (Peng et al. 2007; Peng and Jing 2014). To fill this gap, we performed short-term (up to two months) anoxic hydrothermal experiments at 80°C by reacting synthetic glass powder of a composition similar to the primitive chondrite matrix, metal iron, and olivine with S-rich and S-free fluids. Specific attention was paid to the mineralogical and chemical characterization of the reaction products and the implications for the alteration conditions of CM chondrites.

MATERIAL AND METHODS

"Synthetic GEMS-like" glass preparation

Pristine CM chondrite matrix is mainly composed of amorphous silicate grains a few hundred nanometers in size that share many similarities with GEMS grains (glass with embedded metal and sulfides) observed in chondritic interplanetary dust particles (IDPs) (Bradley 1994; Keller and Messenger 2011; Leroux et al. 2015). We thus used an analogous starting material for our hydrothermal experiments. Synthetic glass (hereafter "synthetic GEMS-like glass") containing 51.82 wt.% SiO_2, 25.80 wt.% MgO, 14.63 wt.% Fe_2O_3, 5.59 wt/% Al_2O_3, and 1.88 wt.% CaO (bulk analysis from SARM, Nancy, France), similar to natural GEMS grains (Leroux et al. 2015), was prepared from oxide carbonate powders (SiO_2, $MgCO_3$, Fe_2O_3, Al_2O_3, and $CaCO_3$) at CRPG (Nancy, France). The powder mixture was melted in platinum crucibles at 1550°C for 30 min and quenched in cold water. This quenched glass was crushed to a fine powder (particles of a few microns to a few hundred microns) in an agate mortar and pestle.

GEMS grains in IDPs contain rounded Fe-Ni metal grains believed to have formed in the hot inner regions of the solar protoplanetary disc by heating of amorphous silicate grains in a reduced environment at moderate temperatures (<730 °C, Davoisne et al. 2006). We therefore reduced our glass using the sealed evacuated silica glass method (Skynner and Luce 1971): the synthetic glass powder was loaded into graphite crucibles placed in sealed evacuated silica glass tubes (2×10^{-2} mbar) and heated at 1000°C for three days (**Fig. 1a**). After this reduction stage, a small amount of small beads of metallic iron (i.e., <1 vol.%), with sizes of a few microns to a few tens of microns, was observed in our synthetic glass (**Fig. 1b, c**).

Hydrothermal experiments

Hydrothermal experiments were performed by placing sample mixtures in Teflon® bowls within Parr® non-stirred pressure vessels. To remove oxygen trapped in the porosity of the Teflon® bowls, the bowls were pre-treated with a hydrazine solution (20 ppm N_2H_2) at 200 °C for one day. Oxygen gas was removed from the vessels according to the reaction (Dargent et al. 2015):

$$O_2\ (g) + N_2H_2\ (aq) = 2H_2O\ (aq) + N_2\ (g). \qquad (1)$$

The reactors were then cleaned in a glove box under inert argon atmosphere (<1 ppm O_2) using 1 M HCl and rinsed several times with MilliQ water. The solid starting products (i.e., 1 g comprising (i) synthetic GEMS-like glass, (ii) San-Carlos olivine [$Mg_{1.8}Fe_{0.19}Ni_{0.01}SiO_4$] grains typically in the size range 20–50 µm, and (iii) spherical iron metal blobs <10 µm in diameter from Sigma Aldrich) were mixed in various proportions (see **Table 1 and Fig. 2a**) under inert Ar atmosphere in the glove box. The sample mixtures were then loaded together with 10 mL of a synthetic saline solution (2.1 mM NaCl, 0.4 mM $MgCl_2$ and $CaCl_2$, pH = 6.5 at 25°C, **Table 1**) into the Teflon® Parr® bombs (**Fig. 2b**).

Previous laboratory experiments demonstrated that tochilinite and cronstedtite preferentially precipitate under alkaline S-rich (the best tochilinite specimens at pH ≈ 11; Kozerenko et al. 2001) and neutral S-free environments (pH ≈ 7; Pignatelli et al. 2013), respectively. Hence, we separated our experiments into two sets: the first with an alkaline environment created by adding 10 mM Na_2S to the initial saline solution (pH = 11.5 at 25°C) and the second with a circumneutral environment employing only the initial salty solution (pH = 6.5 at 25°C, **Table 1**, **Fig. 2b**). The water/rock ratio was set to 10 (by weight) and the vessels were heated at 80°C and at saturated vapor pressure in a furnace for 30 or 60 days. The two sets of experiments are summarized in **Table 1** and in **Figure 2**.

At the end of the experiments, the vessels were removed from the furnace and quenched in cold water. The vessels were opened and the solid products were dried in a glove box under argon atmosphere at room temperature.

Solution analysis

The run solutions were immediately extracted from the vessels after quenching, filtered at 0.02 µm, and separated into two distinct aliquots for (i) pH measurement at room temperature, and (ii) inductively coupled plasma optical emission spectrometry (ICP-OES) analyses. ICP-OES analyses were performed after dilution in HNO_3 (2 vol.%) to determine the concentration of dissolved Al, Ca, Fe, K, Mg, Na, and Si (detection limit < 50 µg/L). Because dissolved Al, Fe, and Mg were below the detection limit in run solutions G-2, GO-2, and GOI-2, additional aliquots (without dilution) were collected and measured by inductively coupled plasma mass spectrometry (ICP-MS) at SARM (Nancy, France) with a detection limit < 1 µg/L.

Characterization techniques

Back-scattered electron (BSE) images of the solid products were obtained at GeoRessources (Nancy, France) using a JEOL J7600F Field Emission Scanning Electron Microscope (FE-SEM) equipped with an Oxford EDS (Energy Dispersive X-ray spectrometer). SEM observations were performed with an accelerating voltage of 15 kV. EDS analyses were made with an accelerating voltage of 15 kV and a beam current of 100nA. Chemical analyses were calibrated using the following natural minerals: albite for Al, hematite for Fe and O, olivine for Mg, orthoclase for Si, wollastonite for Ca and FeS_2 for S.

Solid products were prepared for transmission electron microscopy (TEM) and scanning transmission electron microscopy (STEM) by crushing them in an agate mortar, dispersing them in an ethanol solution under ultrasonic treatment, and evaporating the solution on a holey carbon film placed on a 200 mesh copper grid. TEM imaging, EDX analyses and selected area electron diffraction (SAED) were performed at IJL (Nancy, France) using a JEM-ARM 200F cold-field emission gun TEM/STEM operating at 200 kV and equipped with a spherical aberration (Cs) probe corrector (0.19 and 0.078 nm point resolution in TEM and STEM mode, respectively). Qualitative measurement of elements was obtained using the Cliff-Lorimer ratio method. Electron-transparent cross-sections of samples from GS-2 and GOS-2 were prepared by using a FEI Versa 3D DualBeam field emission (FIB/SEM) at the F.M.E company (Nancy, France).

The hydrated/porous nature and the small sizes (less than 1 µm) of the secondary mineral phases synthesised during our hydrothermal experiments make the SEM-EDS analyses difficult. However, we excluded all the analyses with a total lower than 65 wt.% (lowest total measured in the Fe, Si-rich layer in the S-bearing experiments) and higher than 102 wt.%. In addition, all the representative chemical compositions reported in the Tables S1 and S3 were normalized to 100%.

X-ray diffraction (XRD) data were collected at room temperature with a PANalytical X'pert PRO diffractometer (goniometer θ-2θ), using a Cu tube, a Ge (111) incident-beam monochromater (λ = 1.5406 Å) and a X'Celerator detector (scanning line detector 1D, 2.122° active length) at CRM laboratory (University of Lorraine, France). X-ray patterns were collected on bulk-rock samples, with 2.122° active length, using a scan step of 0.0167° (2θ) and a time of measurement for each sample of 90min, $2\theta_{min}$ = 5° to $2\theta_{max}$ = 70°.

35 kV accelerating voltage and 45 mA current (CRM laboratory, University of Lorraine, France). X-ray patterns were collected on bulk-rock samples, using a scan step of 0.007° (2θ) and a time of measurement for each sample of 90min, $2\theta_{min}$ = 5° to $2\theta_{max}$ = 70°.

RESULTS

Circumneutral S-free experiments

Solid phase characterization

Alteration of primary phases

SEM observations of olivine and synthetic GEMS-like grains do not reveal obvious signs of dissolution on grain surfaces or along grain boundaries (e.g., disk-shaped grains or the formation of a gel layer) at micrometer scale (**Fig. S1**). However, this lack of evidence does not exclude minor signs of dissolution at nanometer scale, but further FIB–TEM investigations are required. In contrast, corrosion textures characterized by thin layers of newly formed material are present at the edges of iron metal grains (**Fig. 3b**).

Secondary mineral paragenesis

SEM-TEM observations of the S-free run products reveal the presence of two new mineral phases synthesized during the hydrothermal experiments. The first is present in the run products of all three S-free experiments and is composed of a fibrous Fe-Si-rich mineral occurring in layers <1 µm thick around native iron metal (**Fig. 3b**). This phase has a composition close to berthierine or greenalite (n = 2, **Fig. 3c, Table S1**).

The second new phase is an iron oxide that occurs only in experiment GOI as grains of a few tens of microns (**Fig. 3a**). This phase is easily identifiable at contacts with iron metal grains. SEM-EDS analyses indicate that this iron oxide has a composition close to goethite: 65.4 ± 2 wt.% Fe, 31.1 ± 1.5 wt.% O, 3.2 ± 0.5 wt.% Si, 0.1 ± 0.3 wt.% Mg, and 0.03 ± 0.1 wt.% Ca (n = 11, 1σ errors; **Fig. 3c, Table S1**).

Cronstedtite precipitation

Detailed TEM investigation of experiment GOI reveals rare triangular crystals of cronstedtite <1 µm in size that were not detected by X-ray diffraction (XRD) (**Fig. 4a, b**). Cronstedtite was not detected in the products of experiments G and GO. TEM-EDS measurements show that these crystals contain of 52.8 ± 1.9 wt.% Fe, 36.9 ± 1.7 wt.% O, 8.3 ± 0.4 wt.% Si, 1.4 ± 0.2 wt.% Al, 0.4 ± 0.1 wt.% Mg, and 0.2 ± 0.1 wt.% Ca (n = 6, 1σ errors; **Fig. 4a, Table S1**). To calculate the average structural formula of cronstedtite, the Fe^{3+}/Fe^{2+} ratio was adjusted to set the occupancy of the octahedral sites to 3 following

Pignatelli et al. (2013). Hence, based on a total of 7 oxygen atoms, we obtained the mean empirical formula of cronstedtite to be $(Fe^{2+}_2Fe^{3+}_{0.9}Mg_{0.1})(Si_{1.1}Al_{0.2}Fe^{3+}_{0.7})O_5(OH)_4$. The SAED pattern along the [001] zone axis of cronstedtite (**Fig. 4d**) reveals: (i) strong h – k = 3n diffractions (e.g., 110, 300, in hexagonal indexing) and weak h – k ≠ 3n diffractions (e.g., 100, 010, 200), and (ii) a hexagonal cell with parameters a = b = 0.54 nm (**Fig. 4c, d**). The SAED pattern along the [010] zone axis indicates the cell parameter c = 0.71 nm (**Fig. 4e, f**), consistent with typical terrestrial (Hybler et al. 2000) and meteoritic cronstedtite (i.e., polytype 1*T*; Pignatelli et al. 2018).

Solution chemistry

The evolution of Si, Ca, Mg, and Fe concentrations in the neutral S-free experiments are presented in **Fig. 5a–c** and **Table S2**. After two months, Si concentrations reached a steady state (within errors) at 0.8 and 0.4 mM in experiments G and GOI, respectively (**Fig. 5a, c**). In experiment GO, the Si concentration increased to 1.2 mM after one month, then decreased to 0.6 mM after two months (**Fig. 5b**). Calcium concentrations remained rather constant at ~0.3 mM in experiments G and GO and at ~0.25 mM in experiment GOI (**Fig. 5a–c)**. Magnesium concentrations decreased from 0.4 to ~0.05 mM over two months in all S-free experiments (**Fig. 5a-c**). Iron and Al concentrations remained very low, ~10^{-4} to 10^{-3} mM, after two months in all the experiments (**Fig. 5a–c**, **Table S2**). The elevated Fe concentrations (from 23 to 78 mM) after one month are surprising and may reflect a strong solution disequilibrium with respect to Fe-bearing minerals (e.g. magnetite, greenalite and cronstedtite) expected to be stable under our experimental. Indeed, thermodynamic simulations performed with PhreeqC software together with the llnl database indicate that dissolved iron concentration should remain within the 10^{-4} to 10^{-6} mM range under our experimental conditions (i.e., T = 80°C, pH = 6–8 and log fO_2 = -60) if the fluid is in equilibrium with magnetite, greenalite or cronstedtite. Thus, the elevated Fe concentrations observed in our run solutions either result from (i) a precipitation delay of Fe-bearing minerals (causing an oversaturation of Fe) or (ii) a contamination/filtration issue. In the absence of a continuous monitoring of solution composition over time, it is difficult to provide a robust explanation for this observation.

The pH of the solutions increased progressively up to pH = 8 in experiments GO and GOI, but decreased slightly to pH = 6 in experiment G (**Fig. 5d; Table S2**).

Alkaline, S-rich experiments

Solid Phase characterization

Alteration of primary phases

SEM observations of the primary phases after reaction do not reveal obvious signs of dissolution on olivine and synthetic GEMS-like grains at the micrometer scale (**Fig. S1**). In contrast, a thin (1–2 µm) iron oxide layer penetrates the surfaces of iron metal grains.

Secondary mineral paragenesis

SEM observations of products of the S-bearing experiments show newly formed synthetic assemblages 2–3 µm thick around iron metal beads (not detected by XRD analysis) (**Fig. 6a, b**). This mineral assemblage can be separated into three different layers according to the textures observed: (i) a compact layer penetrates the metal grains and exhibits irregular contacts with the iron metal, (ii) a secondary rim with an acicular/fibrous texture surrounds the compact layer, and (iii) a fibrous layer surrounds the acicular layer (**Fig. 6a, b**).

The TEM chemical profile of the alteration rims in the GS-2 FIB-produced cross section (**Fig. 7a, e**) shows chemical zoning of Fe, O, S, and Si within the different layers (**Fig. 7b–e**). The inner compact zone (Z_1) is Fe- and O-rich (**Fig. 7c**) and is characterized by homogeneous Fe, O, Si, and S concentrations averaging 61.6, 29.8, 4.8, and 3.7 wt.%, respectively (n = 3, **Fig. 5c**). The acicular/fibrous layer (Z_2) is Fe- and S-rich is compositionally zoned: Fe and S concentrations are highest in the center of the layer (67.5 and 23.2 wt.%, respectively) and decrease towards the surrounding layers (down to ~62 and 9.5 wt.%, respectively), whereas O and Si concentrations are lowest in the center of the layer (8.4 and 0.9 wt.%, respectively) and increase towards the surrounding layers (reaching 24.5 and 4 wt.%, respectively) (n = 5, **Fig. 7e**). The outer zone (Z_3) is also Fe- and O-rich, but contains higher O and Si concentrations (39.4 and 10.6 wt.%, respectively) and lower Fe and S concentrations (49.3 and 0.7 wt.%, respectively) than layers Z_1 and Z_2 (**Fig. 7e**). A layer similar to Z_3 occurs between layers Z_1 and Z_2 with variable thickness (**Fig. 7a–d**).

Tochilinite precipitation

TEM imaging of the acicular Fe-S-rich layer (Z_2) indicate that this assemblage comprises many needle-shaped crystals several hundreds of nanometers in size (**Fig. 8a, b**). High-resolution TEM (HRTEM) images suggest that these crystals grew perpendicular to the

surface of the iron metal grain (**Fig. 8b–c**). However, the corresponding SAED pattern (collected from a small area of the needle-shaped crystals) indicates that this assemblage is poorly crystalline and shows several strong and weak broad rings at *d*-spacings of 0.54, 0.27, 0.25 and 0.18 nm, compatible with tochilinite reflections (**Fig. 8d**; Organova et al. 1973; Pekov et al. 2013). Furthermore, HRTEM images indicate lattice fringes of 0.54 nm and SAED patterns show strong (002) diffraction spots along the c* axis consistent with tochilinite (**Fig. 8e, f**) (Mackinnon and Zolensky 1984; Organova et al. 1988; Kakos et al. 1994). EDX analyses of isolated acicular crystals show that they contain variable concentrations of Fe and O, with the average composition 57.9 ± 9.4 wt.% Fe, 18.4 ± 5.7 wt.% O, 17.9 ± 1.5 wt.% S, 3.9 ± 2 wt.% Si, 0.7 ± 0.8 wt.% Ca, and 0.6 ± 0.8 wt.% Mg (n = 6, 1σ errors; **Fig. 6c**, **Table S3**). These analyses demonstrate that the acicular crystals forming the intermediate rims around iron grains are tochilinite with a mean empirical formula equivalent to $2(Fe_{0.88}S) \cdot 2.1(Fe_{0.96}Mg_{0.04})(OH)_2$ when normalized to 2 S atoms.

Solution chemistry

Si and Ca concentrations of the experimental solutions are plotted as a function of elapsed time in **Fig. 9a–c** and **Table S2**. Si concentrations in the solution increased over two months to reach a steady state (within error) at 1.7 and 1.9 mM in experiments GS and GOS, respectively (**Fig. 9a, b**). In experiment GOIS, the Si concentration increased to 1.1 mM after one month, then decreased to 0.3 mM after two months (**Fig. 9c**). Ca concentrations decreased from 0.4 mM to 0.01–0.02 mM after two months in all the S-bearing experiments (**Fig. 9a–c**). Fe, Mg, and Al concentrations are very low, with most measurements below the ICP-OES detection limit (i.e., <50 µg/L, **Table S2**).

The pH of the S-rich alkaline solutions decreased from 11.5 to 7.7 and 8.8 over two months in experiments GS and GOS, respectively (**Fig. 9d**). In experiment GOIS, the pH decreased to 6.4 after one month, then increased to 9.7 after another month (**Fig. 9d**).

DISCUSSION

These low temperature hydrothermal experiments aimed to investigate the formation of meteoritic tochilinite and cronstedtite from starting products similar to the constituents of the matrices of the most pristine CM chondrite. We first explore the conditions of formation of tochilinite and cronstedtite by comparing our results to previous works on TCIs in CM chondrites and from laboratory experiments. We then estimate the temperatures of formation of CM tochilinite based on their Mg concentration and discuss the implications of these temperatures on understanding the thermal evolution of the CM parent body. We finally conclude the discussion by considering the possibility that tochilinite and cronstedtite may co-precipitate under similar physicochemical conditions for at least a short time.

Conditions of cronstedtite formation

Cronstedtite crystals formed only in the experiment with the highest Fe content (with GEMS-like grains, forsterite, and Fe^0 in equal proportions by mass; $Fe_{tot}/Si = 2.7$). This result is in good agreement with the preferential formation of 1:1 (TO) iron phyllosilicates (i.e., cronstedtite/greenalite) reported for experiments with Fe/Si ratios of 2.25, whereas experiments with lower Fe/Si (i.e., 0.75) produced 2:1 (TOT) iron phyllosilicates (Mizutani et al. 1991). It thus appears that the Fe/Si ratio could be a key parameter controlling the formation of cronstedtite, with the presence of Fe^0 imposing reducing condition (H_2 is a by-product of Fe° oxidation under anoxic conditions) and providing Fe^{2+} for cronstedtite precipitation. In addition, experiments and thermodynamic modeling have shown that cronstedtite crystals form under specific conditions: pH = 7–8, log $fO_2 \approx$ –65 to –60 (estimated from the measured Si concentrations in solutions from experiment GOI and the calculated stability field of cronstedtite at 80°C from Pignatelli et al. 2014, **Fig. 10**), and below 100°C because the stability field of cronstedtite decreases with increasing temperature (**Fig. 10**; Rivard 2001; Schulte and Shock 2004; McAlister and Kettler 2008; Zolotov 2014; Pignatelli et al. 2013, 2014).

Our results indicate that the cronstedtite formed by reaction between synthetic GEMS-like glass, metallic iron, and water. Similarly, in the least altered CM chondrite Paris (Hewins et al. 2014, Marrocchi et al., 2014), (i) the occurrence of platy cronstedtite in association with amorphous silicates and serpentines and (ii) the progressive iron enrichment of the matrix

resulting from the dissolution of Fe-Ni metal beads (Leroux et al. 2015) suggest that cronstedtite formed from fluid reaction with matrix amorphous silicates, Fe-Ni metal beads, and water (melted accreted ices) in CM chondrites.

In CM chondrites, cronstedtite-like crystals probably correspond to a ternary solid solution and/or mixture between greenalite ($(Fe^{2+}Fe^{3+}Mg\square)_3(SiAl)_2O_5(OH)_4$; Guggenheim et al. 1982), chrysotile ($Mg_3Si_2O_5(OH)_4$) and cronstedtite end members (Velbel 2014, Pignatelli et al. 2015). However, pure cronstedtite (i.e., cronstedtite with crystallo-chemical characteristics similar to those reported for terrestrial one) has recently been identified and characterized in CM Paris (Pignatelli et al. 2017, 2018). The chemical composition of our synthetic cronstedtite is in good agreement with both terrestrial and pure cronstedtite in CM Paris (Hybler et al. 2000; Pignatelli et al. 2018) (see **Fig. 3c**). Thus, cronstedtite in CM Paris probably formed under similar conditions to those investigated herein: i.e., high Fe/Si ratio (resulting from the progressive incorporation of Fe into the matrix by dissolution of iron metal/kamacite and Fe-sulfide grains and precipitation of Fe-rich phyllosilicate, Leroux et al. 2015), ~80°C, and in a circumneutral environment (pH = 7–8).

Experimental and natural conditions of tochilinite formation

Condition of tochilinite formation

Few studies have succeeded in synthesizing (Fe,Mg)-tochilinite with Fe and Mg concentrations similar to those in meteoritic tochilinite (see overview in **Tables 2** and **S4**; Kozerenko et al. 1996, 2001; Chistyakova et al. 2006). In CM chondrites, tochilinite is Fe-rich (40–58 wt.% Fe) and the Mg content of its brucite/amakinite-like layer is low (1–5 wt.% Mg, **Table S4**; Palmer and Lauretta 2011; Pignatelli et al. 2017). Kozerenko et al. (1996) produced Fe-rich tochilinite in low temperature (80°C) hydrothermal experiments by depletion of Mg in solution. Chistyakova et al. (2006) and Gubaidulina et al. (2007) synthesized Fe-rich tochilinite crystals in multiple series of experiments at 160–180°C with various Mg contents in the initial mixture (0.67–4.17 mmol; Gubaidulina et al. 2007), but yielded minor Mg contents in the brucite layer (nMg = 0.02–0.36, where nMg is Mg content in the brucite layer normalized to 1 S). However, in these laboratory studies, iron was directly supplied in solution as dissolved Fe^{2+} ($FeCl_2$ solution) and not by dissolution of Fe-Ni metal beads as is the case in primitive chondritic material. Furthermore, these studies do not provide the source of Mg in their starting products (Kozorenko et al. 2001; Chistyakova et al. 2006;

Gubaidulina et al. 2007).

We produced tochilinite from the alteration of synthetic glass and metallic iron, valuable analogues of the amorphous silicates and Fe-Ni metal beads found in CM chondrite matrices (Leroux et al. 2015). Dissolution of our synthetic glass is confirmed by the presence of dissolved Si in all run solutions, especially experiments using only GEMS-like glass as the starting material (**Table S2**), and the presence of Al in all S-free run solutions. We also noted that Si concentrations are higher in S-bearing than S-free experiments, whereas the opposite is observed for Mg (see **Table S2**). The difference in Si concentration is probably related to the different pH values of the initial solutions, as glass dissolution increases with increasing pH in neutral-alkaline conditions (Declercq et al. 2013; Vienna et al. 2018), whereas the dissolved Mg concentration is controlled by the precipitation of secondary Mg-bearing minerals such as brucite (not detected) and/or tochilinite in S-bearing alkaline environments (Zolotov 2014).

Tochilinite synthesized in this study displays chemical and textural similarities to meteoritic tochilinite, such as (i) low Mg content (0–1.9 wt.% or 0.5 ± 0.7 wt.% Mg, 1σ, n = 6, **Table S4**), (ii) acicular morphology (**Fig. 8b**, Lee and Ellen 2008; Haack et al. 2012), and (iii) preferential occurrence around iron metal grains (**Figs. 6a, b and 7a**; Palmer and Lauretta 2011). To our knowledge, this is the first time that tochilinite has been synthesized with characteristics so close to those of meteoritic tochilinite and from experimental conditions analogous to those of CM chondrite alteration. Peng and Jing (2014) also precipitated tochilinite from synthetic (Fe-, Mg-, Si-, Al-, and Ni-rich) metal particles under high pH and S concentrations (pH = 13–14, $[S^{2-}] = 10^{-2}$ to 10^{-1} mol/L) at 110–160°C, but their synthetic mineral contained more Mg (nMg = 0.46, 1σ = 0.1, n = 4) than CM tochilinite.

In CM chondrites, most tochilinite in Type-I TCIs formed during the earliest stages of alteration from dissolution of kamacite by a S-rich fluid under alkaline conditions and temperatures up to 130°C (Mackinnon and Zolensky 1984; Kozerenko et al. 2001; Palmer and Lauretta 2011; Pignatelli et al. 2016, 2017). In our S-bearing experiments, Fe-rich tochilinite systematically surrounds iron metal grains, regardless of the starting materials and the proportion of metallic iron (**Fig. 6a, b**). Based on our SEM and TEM observations, we propose that the formation of tochilinite is induced by dissolution-precipitation reactions occurring at the metallic iron (or kamacite)-tochilinite interface as:

$$3.8Fe\ (s) + 0.08Mg^{2+} + 2HS^{-} + 1.84H^{+} + 4.2H_2O = 2(Fe_{0.88}S) \cdot 2.1(Fe_{0.96}Mg_{0.04})(OH)_2\ (s)$$
$$[\text{Tochilinite}] + 3.98H_2\ (g). \quad (HS^{-} \text{ is the dominant sulfur species at pH = 8–11}) \quad (2)$$

Due to the low solubility of secondary iron-bearing minerals, particularly tochilinite, the reaction is Fe-conservative under our experimental conditions, as evidenced by the constant

and very low iron content of the reacting fluids. We also propose that the coupling between iron dissolution and tochilinite precipitation is due to the interplay between substrate-mediated nucleation and solution chemistry at the reaction front (**Figs. 6 and 7**). This is texturally evident, as very small tochilinite crystallites grew inside the native-iron dissolution pits and perpendicular to the reaction front. The proximity of the source and sink of iron suggests that tochilinite nucleates easily and probably grows faster than the rate of iron dissolution.

Tochilinite precipitation leads to a decrease in S concentration (i.e., consumption of all the S initially in the fluid, **Fig. 9d, Table S2**). Once sulfide activity is no longer sufficient to sustain tochilinite precipitation, Fe-Si-rich phyllosilicates are formed around tochilinite (e.g., greenalite and/or cronstedtite). Similarly, the outer parts of Type-I TCI rims in CM Paris are mainly composed of Fe-silicates similar to cronstedtite (Pignatelli et al. 2016), though in our experiments, the Fe-Si-rich fibrous phase bordering tochilinite (**Fig. 6a, b**) is more similar to greenalite than cronstedtite (**Fig. 6c, Table S1**). These textural and chemical arguments provide clear evidence for the fluid-mediated precipitation of tochilinite.

Tochilinite: a proxy of the thermal history of CM chondrites?

The synthetic tochilinite formed during our hydrothermal experiments was almost entirely made up of amakinite layers (i.e., 96% Fe in the hydroxide layer), with minor Mg (4%). Other tochilinite syntheses at 80–130°C show comparable Fe contents, with all Fe in the hydroxide layer (Kozerenko et al. 1996, 2001), whereas those at a temperature of >130°C have 30–70% Mg for n = 1.5–1.9 in the tochilinite formula (Kakos et al. 1994; Kozerenko et al. 2001; Chistyakova et al. 2006; Gubaidulina et al. 2007; Peng and Jing 2014). It has been proposed that Fe-tochilinite is metastable, with a kinetically controlled formation that requires depletion of Mg^{2+} from solution and sufficiently high Fe^{2+} and S^{2-} activities at low temperature (Kozerenko et al. 2001; Peng et al. 2007; Pekov et al. 2013). Nevertheless, Kozerenko et al. (2001) demonstrated that the two main parameters controlling the stability field of tochilinite are sulfide concentration and temperature. At S^{2-} concentrations between 1×10^{-3} and 5×10^{-5} mol/L, Fe-tochilinite is stable up to 130°C, and (Mg,Fe)-tochilinite is the dominant phase at 130–320°C in the mackinawite-magnetite-pyrrhotite paragenesis (Kozerenko et al. 2001). Other experiments above 130°C produced tochilinite with variable nMg contents, ranging from 0.26 at 160-180°C to 0.66 at 200°C, but none with only amakinite layers (Kakos et al. 1994; Kozerenko et al. 2001; Chistyakova et al. 2006; Peng and Jing 2014).

In CM chondrites, tochilinite has low concentrations of Mg, ranging from 1.6 to 4.5 wt% (Palmer and Lauretta 2011; Pignatelli et al. 2017). This difference in composition is also correlated with degree of alteration of CM chondrites, which could reflect more availability of Mg in solution from the dissolution of forsterite/pyroxene precursors (Hanowski and Brearley 2001). Nevertheless, no strong relationships have been established experimentally between the Mg content in the starting products and that in tochilinite (Chistyakova et al. 2006). This discrepancy is evident in the meteoritic tochilinite of CM Paris, which displays only minor Mg in its structural formula (Mg = 1.6 wt%, **Table S4**) although it is thought to have formed by the pseudomorphism of ferromagnesian silicate precursors (Pignatelli et al. 2016, 2017), so there should have been abundant Mg available.

Thus, temperature could be the most important control on the Mg content in the brucite/amakinite-like layer of tochilinite. Plotting the nMg content of the hydroxide layer of synthetic tochilinite as a function of synthesis temperature reveals a positive trend defined by $T = 175.9 (\pm 44.6) \times nMg + 100.4 (\pm 17.3)$ ($r^2 = 0.72$, n = 8) (**Fig. 11, Table S4**). Using this correlation, meteoritic tochilinite with nMg contents of 0.12–0.32 (**Table S4**, Palmer and Lauretta 2011; Pignatelli et al. 2017) correspond to mean precipitation temperatures of 122 ± 38°C for Paris (n = 2), 132 ± 43°C for Murchison (n = 3), 130 ± 50°C for Murray (n = 3), 157

± 48°C for Cold Bokkeveld (n = 2) and 153°C (± 47°C) for Nogoya (n = 1). These temperatures are higher than the predicted range of precipitation temperatures of (i) CM carbonates estimated from bulk and *in situ* oxygen isotopic measurements and 'clumped' isotopes (0–110°C; Clayton and Mayeda, 1984; Benedix et al. 2003; Guo and Eiler, 2007, Verdier-Paoletti et al., 2017) and (ii) cronstedtite deduced from hydrothermal experiments and thermodynamic data (i.e., $50 \leq T \leq 120$°C; Pignatelli et al. 2013, 2014; Zolotov 2014).

These elevated average precipitation temperatures of meteoritic tochilinite indicate that CM carbonates cannot be formed at the same time as meteoritic tochilinite. This result is consistent with petrographic observations that indicate that primary carbonates (i.e., type 1a calcite; Lee et al. 2014) precipitated at the earliest stages of alteration, before their partial or complete replacement by TCIs (Lee et al. 2013; Vacher et al. 2017). Taking together, the formation temperatures and the mineralization sequence of carbonate and tochilinite minerals suggest an increase of the temperature during the duration of aqueous alteration, from 0-70°C for carbonate to 120-160°C for tochilinite (**Fig. 12**). Furthermore, the chemical zoning observed in Type-II TCIs (i.e., the Fe- and S-enrichment at the border and the Fe- and Si-enrichment toward the center; Pignatelli et al. 2016) indicates that cronstedtite may precipitated after tochilinite, due to the decrease of the sulfur activity during the duration of aqueous alteration (Pignatelli at al. 2017). If so, the range of low formation temperatures of cronstedtite implies that this mineral may precipitated during the cooling phase of the CM parent body, between 50 and 120°C (**Fig. 12**). This result is in good agreement with experimental data that demonstrated that the development of crystals of cronstedtite is likely promoted by a temperature decrease during the course of alteration (Pignatelli et al. 2013).

Therefore, the Mg content of tochilinite seems to be a powerful proxy in order estimate the alteration temperature of CM chondrites. However, we note that this correlation is based on a small amount of data and further hydrothermal experiments are needed to better understand the role of the other physiochemical parameters (e.g., pH, W/R ratio, starting assemblage or solution chemistry) in controlling of the Mg content of tochilinite.

Co-precipitation of tochilinite and cronstedtite in CM chondrites?

In CM chondrites, tochilinite has been proposed to precipitate during the first stages of aqueous alteration under very low oxygen fugacity (Browning and Bourcier 1996), neutral-alkaline pH (Kozerenko et al. 1996; Peng et al. 2007; Peng and Jing 2014), and at 80–320°C (Kozerenko et al. 1996, 2001), whereas cronstedtite forms under less reduced conditions than tochilinite due to the presence of Fe^{3+} (Pignatelli et al. 2014), in circumneutral pH environments (Pignatelli et al. 2013), and below 120°C (Lantenois et al. 2005; Lanson et al. 2012; Pignatelli et al. 2013, 2014) (**Fig. 13**). Therefore, it has been proposed that CM chondrite alteration conditions changed during alteration, with the initial precipitation of tochilinite followed by the formation of cronstedtite (Pignatelli et al. 2016). However, tochilinite is frequently observed in close association with cronstedtite in Type-II TCIs at both the micron and the nanometer scales (Mackinnon and Zolensky 1984; Haack et al. 2012; Leroux et al. 2015; Pignatelli et al. 2016, 2017). This complex intergrowth indicates that (i) tochilinite and cronstedtite may co-precipitated under similar physicochemical conditions for at least a short time (Palmer and Lauretta 2011; Pignatelli et al. 2016) and/or (ii) cronstedtite could have replaced tochilinite during the course of alteration. Identifying which of these two scenarios prevailed is not an easy task, because the intergrowth between tochilinite and cronstedtite can be attributed to either of these two processes. Nevertheless, because tochilinite and cronstedtite have been formed under similar physicochemical conditions in our experiments (i.e., 80°C and pH ≈ 8), here we explore the possibility that they both could have been formed at the same time.

We did not observe cronstedtite crystals in our S-bearing experiments, though we expected cronstedtite to form in experiment GOIS due to (i) the similar proportion of starting assemblages as the cronstedtite-producing S-free experiment GOI and (ii) the favorable concentration of Si in the run solutions (**Table S2, Fig. 13**). This lack of cronstedtite formation may have explained by the final alkalinity of the experiment (pH = 9.7) preventing cronstedtite precipitation (Pignatelli et al. 2015) or the reaction time being too short under the experimental conditions to produce abundant cronstedtite of a high degree of crystallinity compared to longer syntheses (**Table 2**).

Nonetheless, the occurrence of tochilinite and cronstedtite at 80°C in the S-rich and S-free experiments, respectively, suggests that both minerals might form at similar aqueous alteration temperatures. Because the stability field of cronstedtite is expected to diminish with increasing temperature (Pignatelli et al. 2014; Zolotov 2014) and cronstedtite was not

observed in experiments at ≥ 150°C (Rivard 2011; Pierron 2011), co-precipitation of tochilinite and cronstedtite implies a restrictive alteration temperature range of 80–120°C (**Fig. 12**). Following the same logic, in our experiments, cronstedtite formed at pH ≈ 7–8 and tochilinite at pH = ~8–11, consistent with previous results for cronstedtite (pH = 7.2–7.6; Pignatelli et al. 2013) and tochilinite (pH = 7.3–11.4; Kozorenko et al. 1996). Thus, co-precipitation of tochilinite and cronstedtite should indicate a circumneutral environment of pH = 7–8.

Quantitative estimation of the redox conditions of tochilinite and cronstedtite co-precipitation is more problematic because, according to thermodynamic modelling, these two minerals do not share a common fO_2 range (**Fig. 13;** Browning and Bourcier 1996; Dyl et al. 2006; Pignatelli et al. 2014). The fO_2 of cronstedtite precipitation is well constrained in our experiments due to the limited variation of Si concentrations in the associated run solutions (i.e., Si ≈ 4 mM, **Table S2**), implying fO_2 conditions in the range log fO_2 = –62 to –58 at 80°C (**Figs. 10 and 13**). However, we cannot directly estimate the fO_2 for our synthetic tochilinite due to the limited available information on its stability. Browning and Bourcier (1996) showed that the stability of Fe-rich tochilinite implies extremely reducing conditions compared to cronstedtite, i.e., log fO_2 = –91 to –85, though this range of oxygen fugacity is relevant at 0°C (Fujiya et al. 2015), too cold for the formation of meteoritic tochilinite. With increasing temperature, the stability fields of Fe-O-S minerals move toward higher fO_2 and fS_2 (Holland 1959), as demonstrated in **Fig. 13**. Thus, above 0°C, the fO_2 of tochilinite precipitation should be above the values estimated by Browning and Bourcier (1996). This interpretation is supported by the high $Fe^{3+}/\Sigma Fe$ ratio measured in CM Paris Fe-rich tochilinite (i.e., 8–15%; Pignatelli et al. 2017), suggesting that precipitation of tochilinite may have occurred under sufficiently oxidizing conditions to incorporate Fe^{3+} into its mineral structure. Consequently, CM tochilinite formation at 120–160 °C (**Fig. 13**) does not require such extremely reduced conditions as at 0°C (Browning and Bourcier 1996). According to our S-bearing experiments, the presence of a magnetite-like phase around iron metal grains suggests log fO_2 values between –73 and –60 at 80°C (**Fig. 13**).

CONCLUSIONS

We have performed low temperature experiments using starting mineral assemblages (reduced glass, San Carlos olivine, metallic iron) close to those observed in the least altered CM chondrites to better understand the alteration conditions of hydrated asteroids. Triangular cronstedtite crystals formed only in S-free circumneutral conditions (pH = 7–8) with the highest Fe content studied (Fe_{tot}/Si = 2.7), suggesting that chondritic cronstedtite crystals likely formed by reaction of matrix amorphous silicates, Fe-Ni metal beads, and water. For the first time, we have synthesized tochilinite similar to meteoritic tochilinite under conditions analogous to CM chondrite alteration. Iron-rich tochilinite systematically surrounds iron metal grains in all our S-bearing experiments, regardless of the starting mineral assemblage and the proportion of metallic iron, indicating that chondritic tochilinite likely formed from the alteration of Fe-Ni metal beads in a S-bearing alkaline environment at low temperature (i.e., < 160°C).

As both tochilinite and cronstedtite precipitated at 80°C in our experiments, these minerals may have formed at similar aqueous alteration temperatures in CM chondrites. Because cronstedtite stability field is expected to diminish with increasing temperature, an expected co-precipitation of tochilinite and cronstedtite requires restrictive alteration conditions: 80–120°C, pH = 7–8, and more oxidized conditions ($\log fO_2 \approx -65$ to -60) than previously estimated for tochilinite. Comparison of our results to other experimental approaches revealed a positive correlation between the Mg content in the hydroxide layer of synthetic tochilinite and temperature. Based on this correlation, we estimated the mean precipitation temperatures of meteoritic tochilinite to be ~120°C for Paris, ~130°C for Murchison and Murray, ~150°C for Nogoya, and ~160°C for Cold Bokkeveld.

Acknowledgments—We are very grateful to Jaafar Ghanbaja and Sylvie Migot for assistance with TEM characterization. We thank Hervé Marmier, Géraldine Kitzinger, and the SARM team for their technical support for solution analyses. Maxime Clément is thanked for his support in the reduction of the synthetic glass with the sealed evacuated silica glass tubes. We are grateful to Pierrick Durant for his assistance with XRD analyses. We are also grateful to Conel Alexander for very constructive review and helpful comments. Isabella Pignatelli is thanked for helpful discussions. Roger Hewins, Martin Lee and associated editor Mike Zolensky are thanked for constructive reviews and comments. This research was funded by

598 l'Agence Nationale de la Recherche through grant ANR-14-CE33-0002-01 SAPINS (PI Yves
599 Marrocchi) and OTELo. This is CRPG contribution #2676.
600

601 # REFERENCES

602 Barber D. J. 1981. Matrix phyllosilicates and associated minerals in C2M carbonaceous
603 chondrites. *Geochimica et Cosmochimica Acta* 45:945–970.

604 Bailey S. W. 1988. Odinite, a new dioctahedral-trioctahedral Fe^{3+}-rich 1:1 clay mineral. *Clay*
605 *Mineral* 23:237-247.

606 Bunch T. E. and Chang S. 1980. Carbonaceous chondrites-II. Carbonaceous chondrite
607 phyllosilicates and light element geochemistry as indicators of parent body processes
608 and surface conditions. *Geochimica et Cosmochimica Acta* 44:1543–1577.

609 Benedix G., Leshin L., Farquhar J., Jackson T., and Thiemens M. 2003. Carbonates in CM2
610 chondrites: constraints on alteration conditions from oxygen isotopic compositions
611 and petrographic observations. *Geochimica et Cosmochimica Acta* 67:1577–1588.

612 Bradley, J. P. 1994. Chemically Anomalous, Preaccretionally Irradiated Grains in
613 Interplanetary Dust form Comets. *Science* 265:925-929.

614 Brearley A. J. 2006. The action of water. In *Meteorites and the early solar system II*, edited
615 by Lauretta D. S. and McSween H. Y. Tucson, Arizona: The University of Arizona
616 Press. pp. 587–624.

617 Brindley, G.W. 1982. Chemical compositions of berthierines – a review. *Clays Clay Miner.*
618 30:153–155.

619 Browning L. B. and Bourcier W. L. 1996. Tochilinite: A sensitive indicator of alteration
620 conditions on the CM asteroidal parent body. Proceedings, 44th Lunar and Planetary
621 Science Conference. pp. 171–172.

622 Chistyakova N.I., Rusakov V.S., Gubaidulina T.V., and Kozerenko S.V. 2006. Investigations
623 of sulfide minerals with layered structure by Mössbauer spectroscopy methods.
624 *ICAME 2005* 66:613–617.

625 Clark B. E., Ziffer J., Nesvorny D., Campins H., Rivkin A. S., Hiroi T., Barucci M. A.,
626 Fulchignoni M., Binzel R. P., Fornasier S., DeMeo F., Ockert-Bell M. E., Licandro J.,
627 and Mothé-Diniz T. 2010. Spectroscopy of B-type asteroids: Subgroups and meteorite
628 analogs. *Journal of Geophysical Research Planets* 115:1-22.

629 Clayton R. N. and Mayeda T. K. 1984. The oxygen isotope record in Murchison and other
630 carbonaceous chondrites. *Earth and Planetary Science Letter* 67:151–161.

631 Cloutis E. A., Hiroi T., Gaffey M. J., Alexander C. M. O'D., and Mann P. 2011. Spectral
632 reflectance properties of carbonaceous chondrites: 1. CI chondrites. *Icarus* 212:180–
633 209.

634 Dargent M., Truche L., Dubessy J., Bessaque G., and Marmier H. 2015. Reduction Kinetics

635 of Aqueous U(VI) in Acidic Chloride Brines to Uraninite by Methane, Hydrogen or C-
636 Graphite under Hydrothermal Conditions: Implications for the Genesis of
637 Unconformity-Related Uranium Ore Deposits. *Geochimica et Cosmochimica Acta*
638 167:11–26.

639 Davoisne C., Djouadi Z., Leroux H., d'Hendecourt L., Jones A., and Deboffle D. 2006. The
640 origin of GEMS in IDPs as deduced from microstructural evolution of amorphous
641 silicates with annealing. *Astronomy & Astrophysics* 448:L1-L4.

642 Declercq J., Diedrich T., Perrot M., Gislason S. R., and Oelkers E. H. 2013. Experimental
643 determination of rhyolitic glass disso- lution rates at 40–200°C and 2 < pH < 10.1.
644 *Geochimica et Cosmochimica Acta* 100:251–263.

645 Dyl K.A., Manning C.E., and Young E.D. 2006. Modelling aqueous alteration of CM
646 carbonaceous chondrites: implications for cronstedtite formation by water-rock
647 reaction. (abstract #2060). 37th Lunar and Planetary Science Conference.

648 Fuchs L. H., Olsen E., and Jensen K. J. 1973. Mineralogy, mineral-chemistry, and
649 composition of the Murchison (C2) meteorite. *Smithsonian Contributions to the Earth*
650 *Sciences* 10:1–39.

651 Fujiya W., Sugiura N., Marrocchi Y., Takahata N., Hoppe P., Shirai K., Sano Y., and
652 Hiyagon H. 2015. Comprehensive study of carbon and oxygen isotopic compositions,
653 trace element abundances, and cathodoluminescence intensities of calcite in the
654 Murchison CM chondrite. *Geochimica et Cosmochimica Acta* 161:101–117.

655 Gubaidulina T. V., Chistyakova N. I., and Rusakov V. S. 2007. Mössbauer study of layered
656 iron hydroxysulfides: Tochilinite and valleriite. *Bulletin of the Russian Academy of*
657 *Sciences: Physics* 71:1269–1272.

658 Guggenheim S., Bailey S. W., Eggleton R. A., and Wilkes P. 1982. Structural aspects of
659 greenalite and related minerals. *The Canadian Mineralogist* 20:1-18.

660 Haack H., Grau T., Bischoff A., Horstmann M., Wasson J., Sorensen A., Laubenstein M., Ott
661 U., Palme H., Gellissen M., Greenwood R. C., Pearson V. K., Franchi I. A., Gabelica
662 Z., and Schmitt-Kopplin P. 2012. Maribo-A new CM fall from Denmark. *Meteoritics*
663 *& Planetary Science* 47:30-50.

664 Hanowski N. P. and Brearley A. J. 2001. Aqueous alteration of chondrules in the CM
665 carbonaceous chondrite, Allan Hills 81002: Implications for parent body alteration.
666 *Geochimica et Cosmochimica Acta* 65:495–518.

667 Hewins R. H., Bourot-Denise M., Zanda B., Leroux H., Barrat J.-A., Humayun M., Göpel C.,
668 Greenwood R. C., Franchi I. A., Pont S., Lorand J.-P., Cournède C., Gattacceca J.,
669 Rochette P., Kuga M., Marrocchi Y., and Marty B. 2014. The Paris meteorite, the least
670 altered CM chondrite so far. *Geochimica et Cosmochimica Acta* 124:190–222.

671 Holland H. D. 1959. Stability relations among the oxides, sulfides, sulfates and carbonates of
672 ore and gangue metals, [Part] 1 of Some applications of thermochemical data to
673 problems of ore deposits. *Economic Geology* 54:184–233.

674 Howard K. T., Alexander C. M. O'D., Schrader D. L., and Dyl K. A. 2015. Classification of

675 hydrous meteorites (CR, CM and C2 ungrouped) by phyllosilicate fraction: PSD-XRD
676 modal mineralogy and planetesimal environments. *Geochimica et Cosmochimica Acta*
677 149:206–222.

678 Howard K. T., Benedix G. K., Bland P. A. and Cressey G. 2011. Modal mineralogy of CM
679 chondrites by X-ray diffraction (PSD-XRD): Part 2. Degree, nature and settings of
680 aqueous alteration. *Geochimica et Cosmochimica Acta* 75:2735–2751.

681 Howard K. T., Benedix G. K., Bland P. A. and Cressey G. 2009. Modal mineralogy of CM2
682 chondrites by PSD-XRD: Part 1. Total phyllosilicate abundance and the degree of
683 aqueous alteration. *Geochimica et Cosmochimica Acta* 73:4576–4589.

684 Hybler J., Petříček V., Ďurovič S., and Smrčok Ĺ. 2000. Refinement of the Crystal Structure
685 of Cronstedtite-1T. *Clays and Clay Minerals* 48:331–338.

686 Jarosewich E. 1990. Chemical analyses of meteorites: a compilation of stony and iron
687 meteorite analyses. *Meteoritics* 25:323–337.

688 Kakos G. A., Turney T. W., and Williams T. B. 1994. Synthesis and structure of tochilinite: A
689 layered metal hydroxide/sulfide composite. *Journal of Solid State Chemistry* 108:102–
690 111.

691 Keller L. P. and Messenger S. 2011. On the origins of GEMS grains. *Geochimica et*
692 *Cosmochimica Acta* 75:5336–5365.

693 Kogure, T., Hybler, J., and Yoshida, H. 2002. Coexistence of two polytypic groups in
694 cronstedtite from Lostwithiel England. *Clays and Clay Minerals* 50:504-513.

695 Kozerenko S.V., Fadeev V.V., Organova N.I., Chstyakova N.I., Kolpakova N.N., and Senin
696 V.G. 2001. Synthesis, formation conditions and crystallochemistry of tochilinites –
697 iron, magnesium and sodium hydroxide-sulfides. *Experiment in Geosciences* 10:57-
698 58.

699 Kozerenko S. V., Organova N. J., Fadeev V. V., Magazina L.O., Kolpakova N. N., and
700 Kopneva L. A. 1996. Tochilinite produced in laboratory. Proceedings, 27th Lunar and
701 Planetary Science Conference. pp. 695–696.

702 Lanson, B., Lantenois, S., Van Aken, P.A., Bauer, A., and Plançon, A. 2012. Experimental
703 investigation of smectite interaction with metal iron at 80ºC: structural
704 characterization of newly formed Fe-rich phyllosilicates. *American Mineralogist*
705 97:864-871.

706 Lantenois, S., Lanson, B., Muller, F., Bauer, A., Jullien, M., and Plançon, A. 2005.
707 Experimental study of smectite interaction with metal Fe at low temperature: 1.
708 Smectite destabilization. *Clays and Clay Minerals* 53:597-612.

709 Lee M. R., Lindgren P. and Sofe M. R. 2014. Aragonite, breunnerite, calcite and dolomite in
710 the CM carboanceous chondrites: High fidelity recorders of progressive parent body
711 aqueous alteration. *Geochimica et Cosmochimica Acta* 144:126–156.

712 Lee M. R., Sofe M. R., Lindgren P., Starkey N. A. and Franchi I. A. 2013. The oxygen
713 isotope evolution of parent body aqueous solutions as recorded by multiple carbonate

generations in the Lonewolf Nunatak 94101 CM2 carbonaceous chondrite. *Geochimica et Cosmochimica Acta* 121:452–466.

Lee M. R. and Ellen R. 2008. Aragonite in the Murray (CM2) carbonaceous chondrite: implications for parent body compaction and aqueous alteration. *Meteoritics & Planetary Science* 43:1219–1231.

Leroux H., Cuvillier P., Zanda B., and Hewins R. H. 2015. GEMS-like material in the matrix of the Paris meteorite and the early stages of alteration of CM chondrites. *Geochimica et Cosmochimica Acta* 170:247–265.

MacKinnon I. D. R. and Zolensky M. E. 1984. Proposed structures for poorly characterized phases in C2M carbonaceous chondrite matrix. *Nature* 309:240–242.

Marrocchi Y., Gounelle M., Blanchard I., Caste F. and Kearsley A. T. (2014) The Paris CM chondrite: Secondary minerals and asteroidal processing. *Meteorit. Planet. Sci.* **49**, 1232–1249.

Marrocchi Y., Bekaert D. V., and Piani L. 2018. Origin and abundance of water in carbonaceous asteroids. *Earth and Planetary Science Letter* 482:23–32.

McAlister, J.A. and Kettler, R.M. 2008. Metastable equilibria among dicarboxylic acids and the oxidation state during aqueous alteration on the CM2 chondrite parent body. *Geochimica et Cosmochimica Acta* 72:233-241.

Mizutani T., Fukushima Y., Okada A., Kamigaito, O., and Kobayashi T. 1991. Synthesis of 1:1 and 2:1 iron phyllosilicates and characterization of their iron state by Mössbauer spectroscopy. *Clays and Clay Minerals* 39:381–386.

Moroz L. V., Kozerenko S. V. and Fadeev V. V. 1997. The reflectance spectrum of synthetic tochilinite. Proceedings, 28th Lunar and Planetary Science Conference. pp. 983-984.

Nakamura T. and Nakamuta Y. 1996. X-ray study of PCP from the Murchison CM carbonaceous chondrite. *Proceeding of the NIPR Symposium on Antarctic Meteorites* 9:37–50.

Organova N. I., Gorshkov A. I., Dikov Yu. P., Kul'bachinskiy V. A., Laputina I. P., Sivtsov A. V., Sluzhenikin S. F., and Ponomarenko A. I. 1988. The new data on tochilinite. *International Geology Review* 6:84–98.

Organova N. I., Drits V. A., and Dmitrik A. L. 1973. Structural study of tochilinite. Part I. The isometric variety. *Soviet Physics - Crystallography* 17:667-671.

Organova N. I., Genkin A. D., Drits V. A., Dmitrik A. L. and Kuzmina O. V. 1971. Tochilinite: A new sulfide hydroxide of iron and magnesium. *Zapiski Vses Mineralogiscogo Obschestva* 4:477-487.

Palmer E. E. and Lauretta D. S. 2011. Aqueous alteration o kamacite in CM chondrites. *Meteoritics & Planetary Science* 46:1587–1607.

Peng Y., Xu L., Xi G., Zhong C., Lu J., Meng Z., Li G., Zhang S., Zhang G., and Qian Y. 2007. An experimental study on the hydrothermal preparation of tochilinite nanotubes

and tochilinite serpentine-intergrowth nanotubes from metal particles. *Geochimica et Cosmochimica Acta* 71:2858–2875.

Peng Y. and Jing Y. 2014. Hydrothermal preparation of analogous matrix materials of carbonaceous chondrites from metal alloy particles. *Meteoritics & Planetary Science* 402:252-262.

Pierron O. 2011. Interactions eau-fer-argilite: Rôle des paramètres Liquide/Roche, Fer/Argilite, Température sur la nature des phases minérales. Ph.D. thesis, Henri Poincaré University, Nancy, France.

Pekov I. V., Sereda E. V., Polekhovsky Yu. S., Britvin S. N., Chukanov N. V., Yapaskurt V. O., and Bryzgalov I. A. 2013. Ferrotochilinite, $6FeS \cdot 5Fe(OH)_2$, a new mineral from the Oktyabr'sky deposit, Noril'sk district, Siberia, Russia. *Geology of Ore Deposits* 55:567-574.

Pignatelli I., Mugnaioli E., and Marrocchi Y. 2018. Cronstedtite polytypes in the Paris meteorite. *European Journal Mineralogy* 30:349-354.

Pignatelli I., Marrocchi Y., Mugnaioli E., Bourdelle F., and Gounelle M. 2017. Mineralogical, crystallographic and redox features of the earliest stages of fluid alteration in CM chondrites. *Geochimica et Cosmochimica Acta* 209:106–122.

Pignatelli I., Marrocchi Y., Vacher L. G., Delon R., and Gounelle M. 2016. Multiple precursors of secondary mineralogical assemblages in CM chondrites. *Meteoritics & Planetary Science* 51:785–805.

Pignatelli I., Vacher L. G., and Marrocchi Y. 2015. Hydrothermal preparation of analogous matrix minerals of CM carbonaceous chondrites from metal alloy particles" by Y. Peng and Y.Jing [Earth Planet. Sci. Lett. 408 (2014) 252–262]. *Earth and Planetary Science Letter* 428:307–309.

Pignatelli I., Bourdelle F., Bartier D., Mosser-Ruck R., Truche L., Mugnaioli E., and Michau N. 2014. Iron-clay interactions: detailed study of the mineralogical transformation of claystone with emphasis on the formation of iron-rich T-O phyllosilicates in a step-by-step cooling experiment from 90°C to 40°C. *Chemical Geology* 387:1-11.

Pignatelli I., Mugnaioli E., Hybler J., Mosser-Ruck R., Cathelineau M., and Michau N. 2013. A multi-technique characterization of cronstedtite synthesized by iron–clay interaction in a step-by-step cooling procedure. *Clays and Clay Minerals* 61:277–289.

Ramdohr P. 1963. The opaque minerals in stony meteorites. *Journal of Geophysical Research* 68:2011–2036.

Rivard, C. 2011. Contribution à l'étude de la stabilité des minéraux constitutifs de l'argilite du Callovo-Oxfordien en présence de fer à 90°C. Ph.D. thesis, Henri Poincaré University, Nancy, France.

Rubin A. E., Trigo-Rodríguez J. M., Huber H., and Wasson J. T. 2007. Progressive aqueous alteration of CM carbonaceous chondrites. *Geochimica et Cosmochimica Acta* 71:2361–2382.

Schulte, M. and Schock, E. 2004. Coupled organic synthesis and mineral alteration on the meteorite parent bodies. *Earth and Planetary Science Letter* 39:1577-1590.

Skynner, B. J. and Luce, D. 1971. Solid Solutions of the type (Ca,Mg,Mn,Fe)S and their use as geothermometers for the enstatite chondrites. *American Mineralogist* 56:1269-1297.

Tomeoka K. and Buseck P. R. 1985. Indicators of aqueous alteration in CM carbonaceous chondrites: Microtextures of a layered mineral containing Fe, S, O and Ni. *Geochimica et Cosmochimica Acta* 49:2149–2163.

Vacher L. G., Marrocchi Y., Villeneuve J., Verdier-Paoletti M. J., and Gounelle M. 2017. Petrographic and C & O isotopic characteristics of the earliest stages of aqueous alteration of CM chondrites. *Geochimica et Cosmochimica Acta* 213:271–290.

Velbel M. A. 2014. Stoichiometric reactions describing serpentinization of anhydrous primary silicates: a critical appraisal, with application to aqueous alteration of chondrule silicates in CM carbonaceous chondrites. *Clays and Clay Minerals* 62:126-136.

Verdier-Paoletti M. J., Marrocchi Y., Avice G., Roskosz M., Gurenko A. and Gounelle M. (2017) Oxygen isotope constraints on the alteration temperatures of CM chondrites. *Earth Planet. Sci. Lett.* **458**, 273–281.

Vienna, J. D., James J. N., Joseph V. R., and Sebastien N. K. 2018. Impacts of glass composition, pH, and temperature on glass forward dissolution rate. *Npj Materials Degradation* 2:22.

Zolensky M. E., Mittlefehldt D. W., Lipschutz M. E., Wang M.-S., Clayton R. N., Mayeda T. K., Grady M. M., Pillinger C., and B D. 1997. CM chondrites exhibit the complete petrologic range from type 2 to 1. *Geochimica et Cosmochimica Acta* 61:5099–5115.

Zolensky M. E. and Mackinnon I. D. R. 1986. Microstructures of cylindrical tochilinites. *American Mineralogist* 71:1201–1209.

Zolensky M. E., Barett R. and Browning L. 1993. Mineralogy and composition of matrix and chondrule rims in carbonaceous chondrites. *Geochimica et Cosmochimica Acta* 57:3123–3148.

Zolotov M. Y. 2014. Formation of brucite and cronstedtite-bearing mineral assemblages on Ceres. *Icarus* 228:13–26.

FIGURE CAPTIONS

Fig. 1. Synthetic GEMS-like glass preparation. a) Schematic representation of the sealed evacuated silica tube method used in this study to reduce our synthetic glass. At time t_1, the silica glass tube was connected to a vacuum pump to evacuate the atmosphere inside the tube. When the pressure reached 2×10^{-2} mbar (time t_2), the silica glass was melted using a torch to seal the tube without breaking the vacuum. b) and c) BSE images of the synthetic GEMS-like material after three days of reduction at 1000°C.

Fig. 2. Overview of the anoxic hydrothermal experiments. a) Initial mixing proportions of the solid starting products and their respective bulk Fe/Si ratio. b) Schematic representation of the loaded autoclaves for the two sets of experiments and summary of the initial parameters.

Fig. 3. Run products from the circumneutral S-free experiments. a) BSE image of run products from experiment GOI-2, showing the occurrence of iron oxide grains of a few tens of microns. b) TEM imaging of a Fe-Si-rich phase located around an iron metal grain in experiment G-1. c) Chemical compositions (wt.%) of the synthetic assemblages produced in experiments GOI-1 and GOI-2 plotted in a Fe-Mg-Si ternary diagram (see Table S1 for details). White diamonds represent the composition of meteoritic cronstedtite from the Paris CM chondrite (Pignatelli et al. 2018). Black circles represent the ideal chemical compositions of berthierine ('Be'; Brindley 1982), cronstedtite ('Cr'; Hybler et al. 2000; Pignatelli et al. 2013), greenalite ('Gr'; Guggenheim et al. 1982), kamacite ('Ka'), and odinite ('Od'; Bailey 1988).

Fig. 4. TEM images and SAED patterns of run products from neutral S-free experiment GOI-2. a) An aggregate of four cronstedtite crystals. b) A single cronstedtite crystal in direct contact with fibrous Fe-rich phyllosilicate. c) and d) TEM image and corresponding SAED pattern along the [001] zone axis of a synthetic cronstedtite. e) and f) TEM image and corresponding SAED pattern along the [010] zone axis of another cronstedtite.

Fig. 5. Evolution of solution chemistry during neutral S-free experiments a) G, b) GO, and c) GOI. Si (magenta), Ca (green), Mg (purple), and Fe (orange) concentrations in the run solutions are shown as a function of elapsed time (error bars are 10%). Al concentrations (not shown) remained low and are reported in **Table S2**. d) pH of the solutions measured at 25°C

856 in experiments G (black open squares and solid line), GO (black solid squares and dashed
857 line), and GOI (gray solid squares and line) shown as a function of elapsed time.
858
859 **Fig. 6.** Run products from alkaline S-bearing experiments. a) and b) BSE images of iron metal
860 beads surrounded by three layers of newly precipitated assemblages in experiment GOS-1.
861 These phases show different textures: (i) an inner compact layer, (ii) an intermediate acicular
862 layer, and (iii) an outer fibrous layer of variable thickness. c) Chemical compositions (wt.%)
863 of the synthetic assemblages produced in experiments G-S and GO-S plotted in a Fe-S-Si
864 ternary diagram (see Table S3 for details). Black circles represent the ideal chemical
865 compositions of cronstedtite ('Cr'; Hybler et al. 2000; Pignatelli et al. 2013), ferrotochilinite
866 ('Fe-To'; Pekov et al. 2013), greenalite ('Gr'; Guggenheim et al. 1982), kamacite ('Ka), and
867 Mg-tochilinite ('Mg-To'; Organova et al. 1971).
868
869 **Fig. 7.** TEM characterization of secondary iron oxide layers around iron metal grains in
870 alkaline S-bearing experiments. a) An iron metal grain from the FIB-produced cross section
871 of samples from experiment GS-2, surrounded by three layers (Z_1, Z_2, and Z_3) of secondary
872 assemblages. The white solid line in (a) represents the location of the TEM chemical profile
873 in (e). b) to d) TEM-EDS maps of Si, Fe, and S distributions in the same area shown in (a). e)
874 TEM chemical profile of Fe, O, S, and Si concentrations corresponding to the white solid line
875 in (a).
876
877 **Fig. 8.** TEM images and SAED patterns of secondary acicular tochilinite around iron metal
878 grains. a) TEM image of the GOS-2 FIB-produced cross section. B) TEM image of the
879 products of the S-bearing experiment around an iron metal bead. c) TEM image of the Fe-S-
880 rich acicular layer from the GS-2 FIB-produced cross section. d) SAED pattern collected from
881 the acicular mineral displayed in (c) showing broad rings of varying intensity that are
882 consistent with natural tochilinite (Organova et al. 1973; Pekov et al. 2013). e) HRTEM
883 image of a acicular tochilinite. f) SAED pattern of tochilinite along the c* axis showing the
884 strong (002) diffraction spots of tochilinite.
885
886 **Fig. 9.** Evolution of solution chemistry during alkaline S-bearing experiments a) GS, b) GOS,
887 and c) GOIS. Si (magenta) and Ca (green) concentrations of the solutions are shown as a
888 function of elapsed time (errors are 10%). Mg, Al, and Fe concentrations (not shown)
889 remained very low and are reported in **Table 2**. d) pH of solutions measured at 25°C in

890 experiments GS (black open squares and solid line), GOS (black solid squares and dashed
891 line), and GOIS (grey solid squares and solid line) shown as a function of elapsed time.
892
893 **Fig. 10.** The stability fields of cronstedtite, greenalite, hematite, and magnetite in log [$Si_{(aq)}$]
894 *vs* *f*(O_2) phase diagrams at 80°C (solid black line and blue shaded field), 100°C, and 150°C
895 (dotted lines) from Pignatelli et al. 2014. The vertical dashed black line corresponds to the Si
896 concentration measured in the run solution of S-free experiment GOI and the red shaded area
897 represents the range of Si concentrations measured in the solutions of S-bearing experiment
898 GOIS.
899
900 **Fig. 11.** Synthesis temperature as a function of Mg content (nMg) in synthetic tochilinite from
901 this study (red circle) and literature (black circles) (**Table S4**; Kakos et al. 1994; Kozerenko et
902 al. 1996, 2001; Chistyakova et al. 2006; Peng and Jing 2014). The blue shaded area represents
903 the nMg values of meteoritic tochilinite (Palmer and Lauretta 2011; Pignatelli et al. 2017) and
904 the associated formation temperatures based on the regression equation T = 175.9 (± 44.6) ×
905 nMg + 100.4 (± 17.3).
906
907 **Fig. 12.** Schematic representation of the expected of ^{26}Al temperature profile of CM chondrite
908 parent body as function of time. The range of temperature formation of calcite (0-70°C, green
909 rectangle) and cronstedtite (50-120°C, blue rectangle) have been taken from the literature
910 (calcite: Clayton and Mayeda 1984, Benedix et al. 2003; Guo and Eiler 2007; cronstedtite:
911 Pignatelli et al. 2013, 2014; Zolotov 2014). Formation age of calcite from Fujiya et al. 2012 is
912 given as indication.
913
914 **Fig. 13.** Log *f*O_2-log *f*S_2 diagram of the Fe-O-S system at 80°C (solid line) and 25°C (dotted
915 line) demonstrating the co-stability field of tochilinite and cronstedtite, modified after Holland
916 (1959). The stability field of tochilinite at 0°C is from Browning and Bourcier (1996).
917

FIGURES

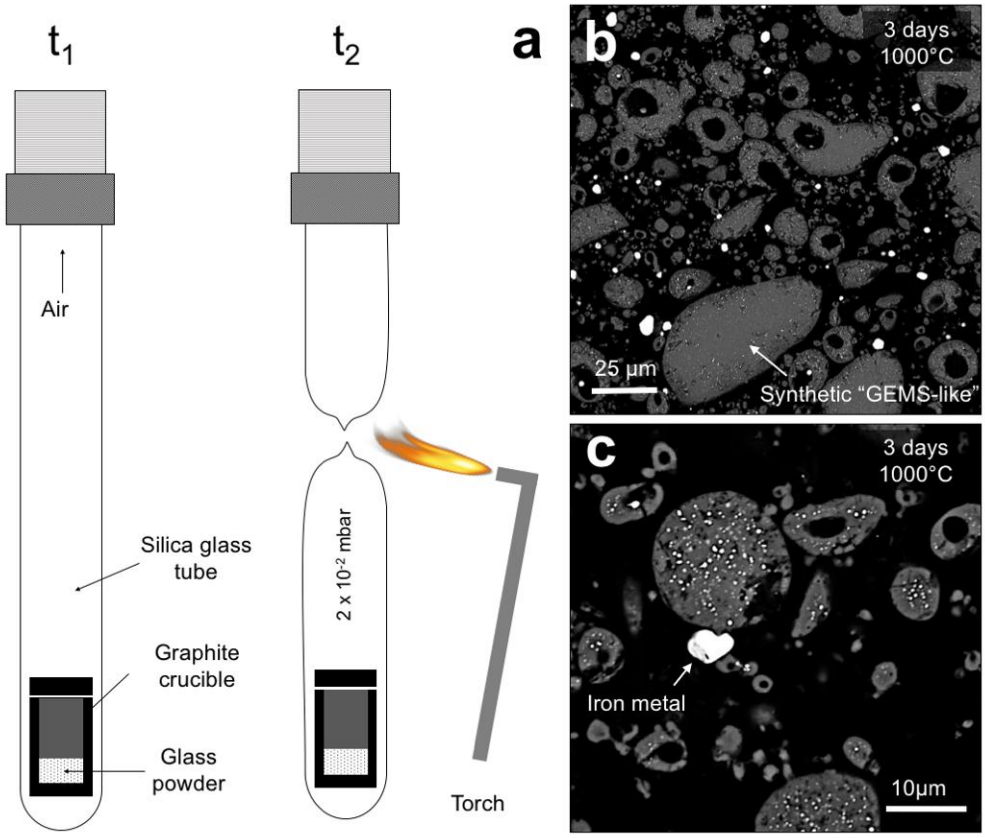

Figure 1

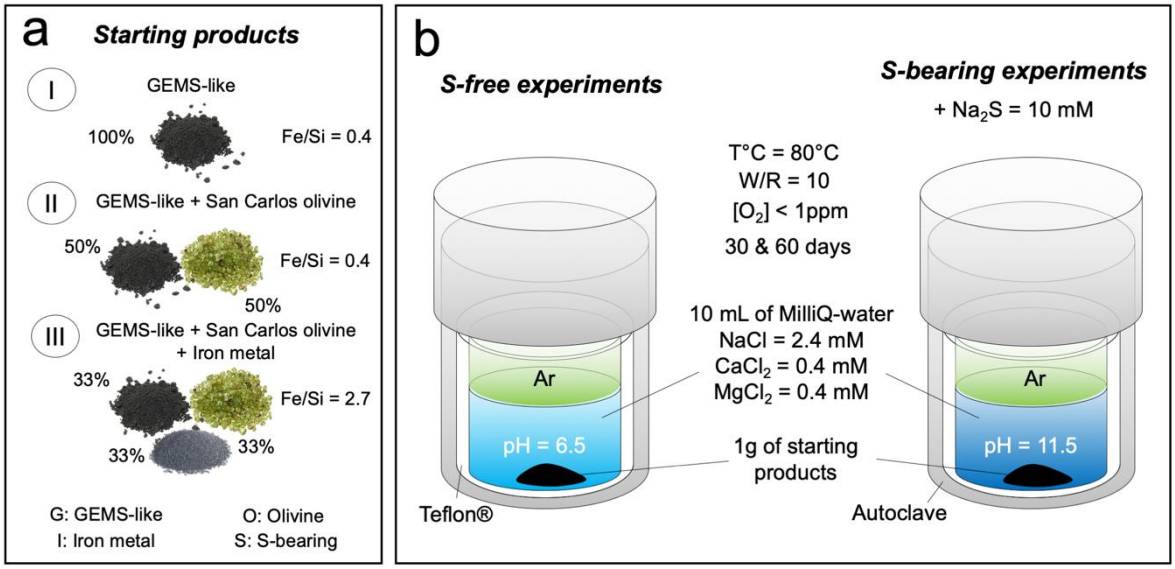
a
Starting products
I
GEMS-like
100%
Fe/Si = 0.4
II
GEMS-like + San Carlos olivine
50%
Fe/Si = 0.4
50%
III
GEMS-like + San Carlos olivine
+ Iron metal
33%
Fe/Si = 2.7
33%
33%
G: GEMS-like
I: Iron metal
O: Olivine
S: S-bearing
b
S-free experiments
S-bearing experiments
+ Na2S = 10 mM
T°C = 80°C
W/R = 10
[O2] < 1ppm
30 & 60 days
10 mL of MilliQ-water
NaCl = 2.4 mM
CaCl2 = 0.4 mM
MgCl2 = 0.4 mM
Ar
pH = 6.5
1g of starting
products
Ar
pH = 11.5
Teflon®
Autoclave

Figure 2

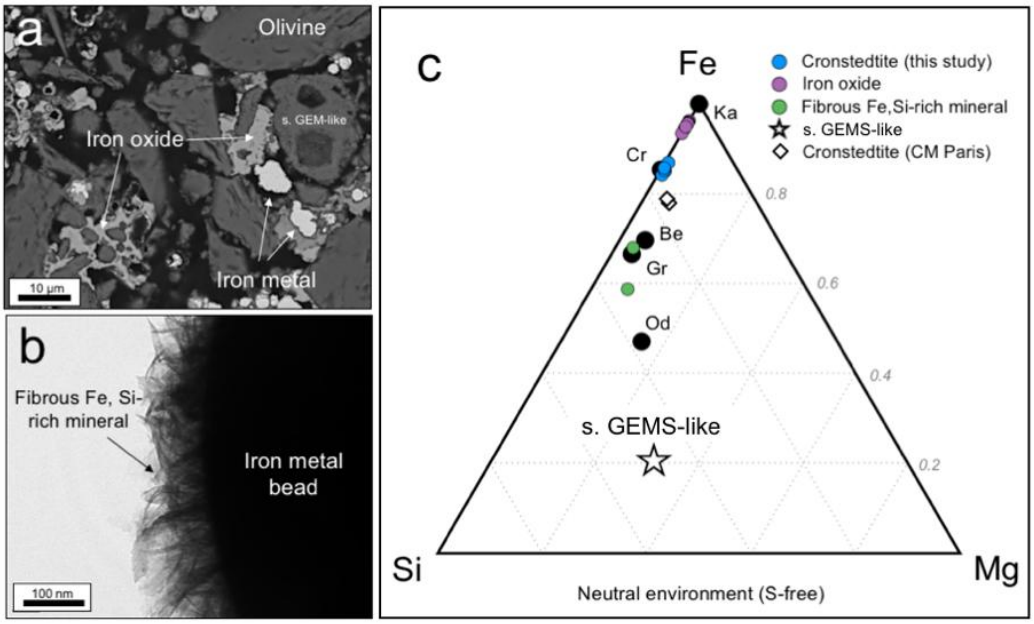
a
Olivine
s. GEM-like
Iron oxide
Iron metal
10 µm
b
Fibrous Fe, Si-rich mineral
Iron metal bead
100 nm
c
Fe
Ka
Cr
Be
Gr
Od
s. GEMS-like
Si
Mg
Neutral environment (S-free)
0.8
0.6
0.4
0.2
Cronstedtite (this study)
Iron oxide
Fibrous Fe,Si-rich mineral
s. GEMS-like
Cronstedtite (CM Paris)

Figure 3

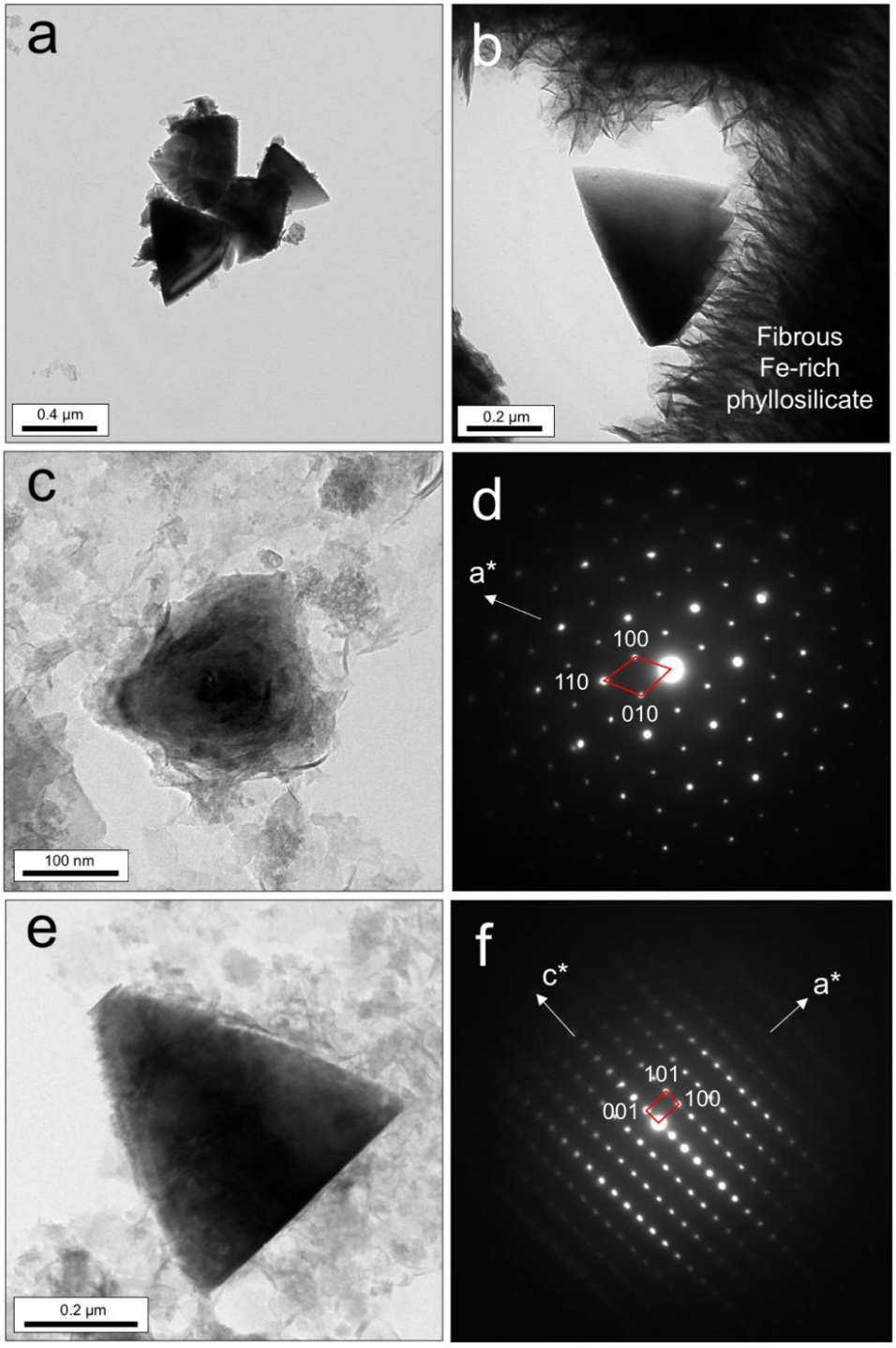
a
0.4 µm
b
Fibrous
Fe-rich
phyllosilicate
0.2 µm
c
100 nm
d
a*
100
110
010
e
0.2 µm
f
c*
a*
101
001
100

Figure 4

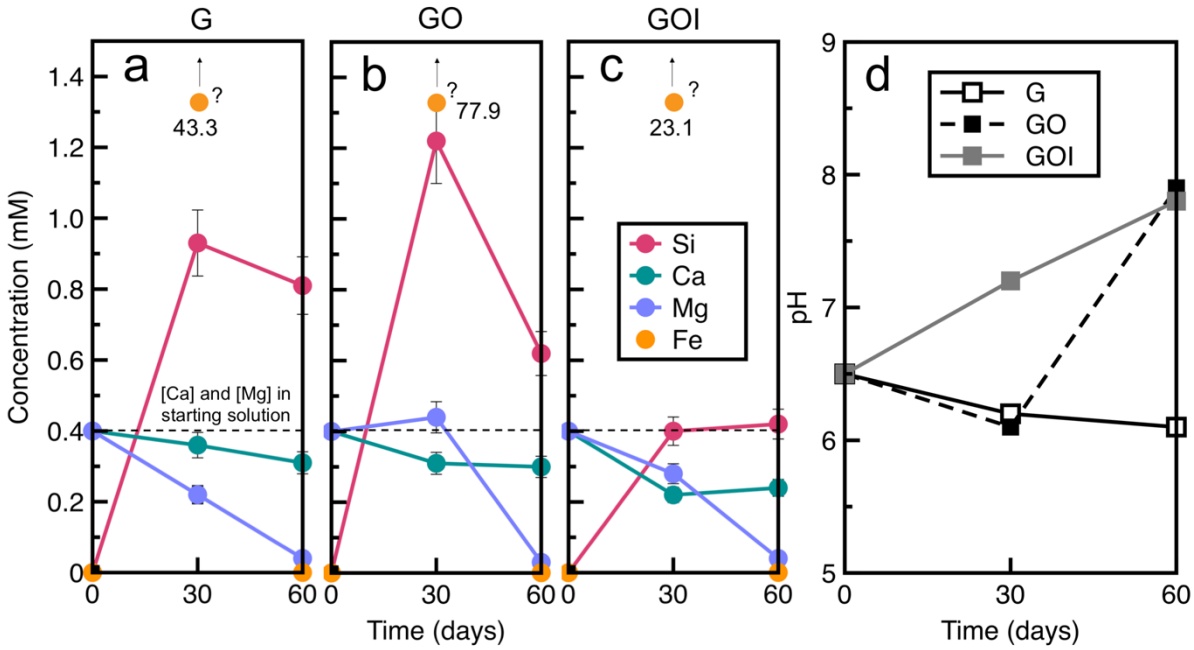

933
934 **Figure 5**
935
936

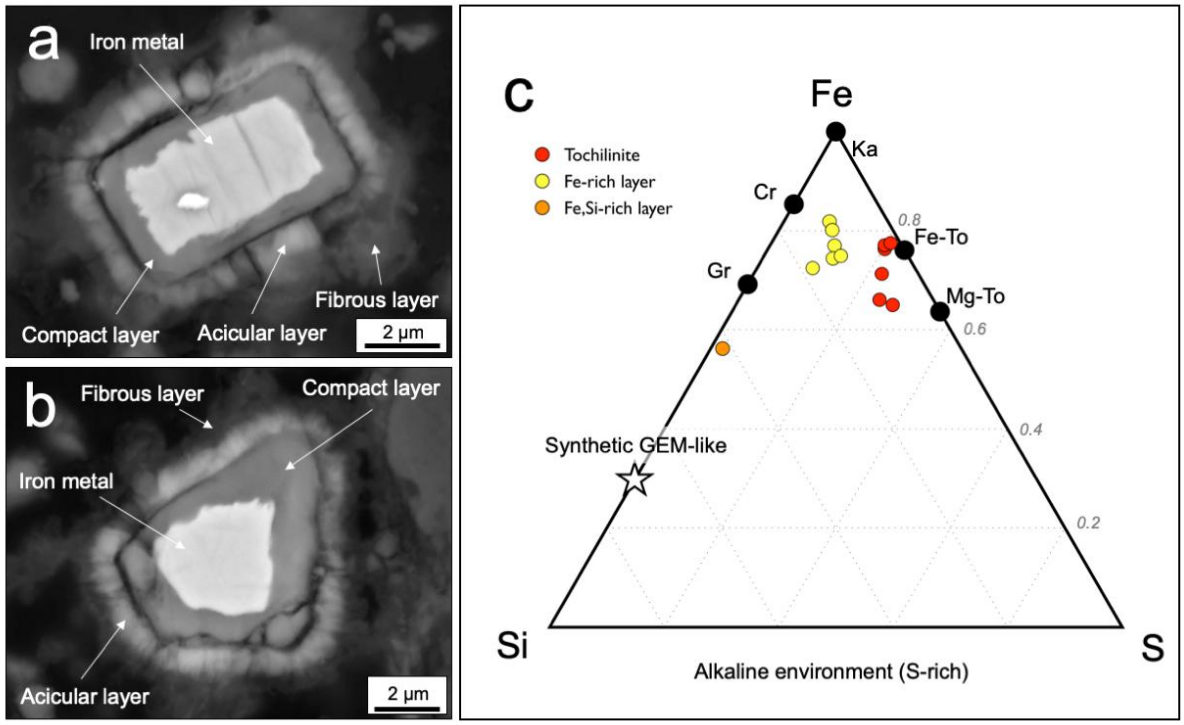
a
Iron metal
Fibrous layer
Compact layer
Acicular layer
2 µm
b
Fibrous layer
Compact layer
Iron metal
Acicular layer
2 µm
C
Fe
Ka
Cr
Gr
Fe-To
Mg-To
0.8
0.6
0.4
0.2
Tochilinite
Fe-rich layer
Fe,Si-rich layer
Synthetic GEM-like
Si
S
Alkaline environment (S-rich)

Figure 6

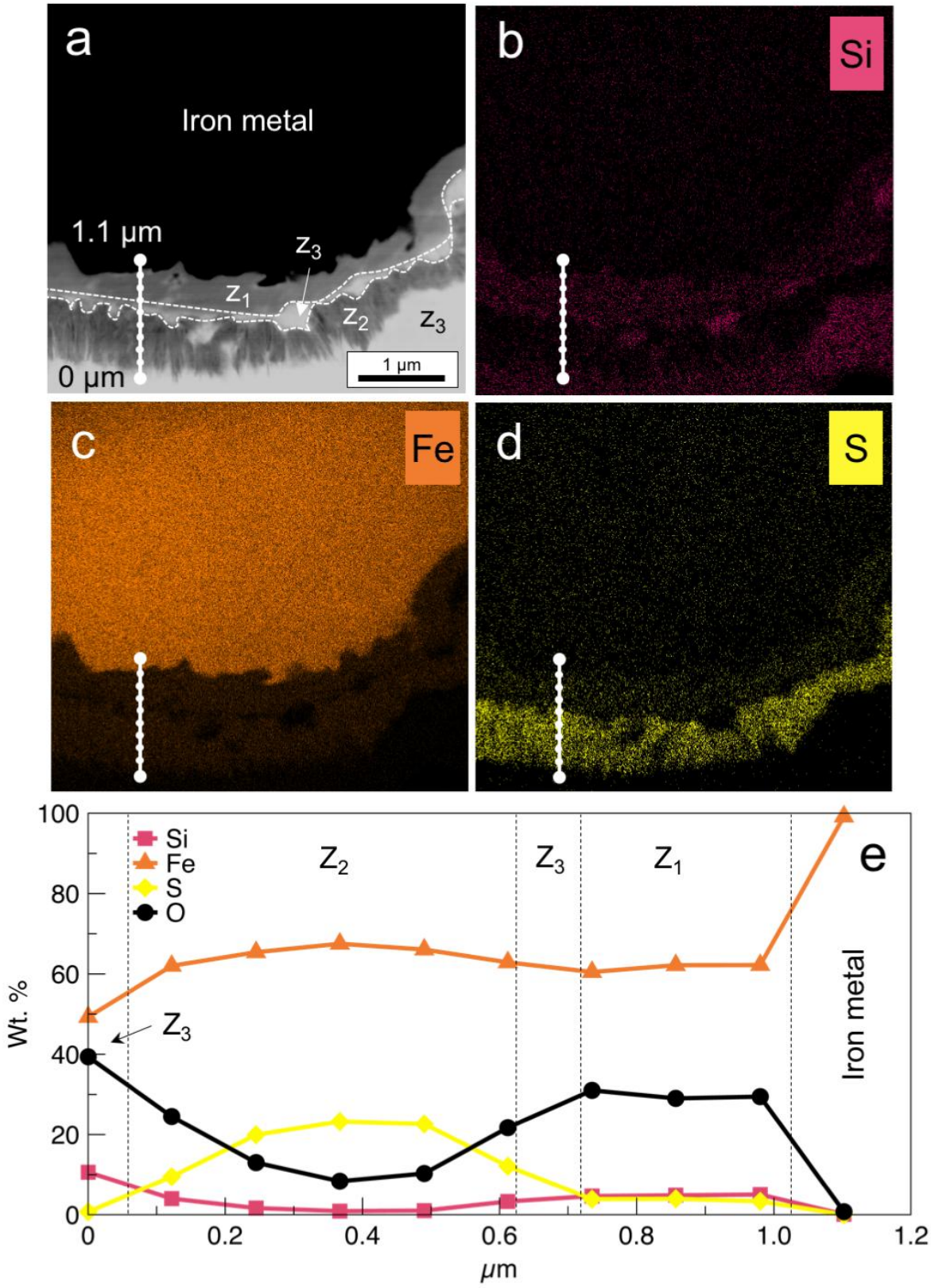
a
Iron metal
1.1 µm
z3
z1
z2
z3
0 µm
1 µm
b
Si
c
Fe
d
S
e
Si
Fe
S
O
Z2
Z3
Z1
Z3
Iron metal
Wt. %
µm
100
80
60
40
20
0
0
0.2
0.4
0.6
0.8
1.0
1.2

Figure 7

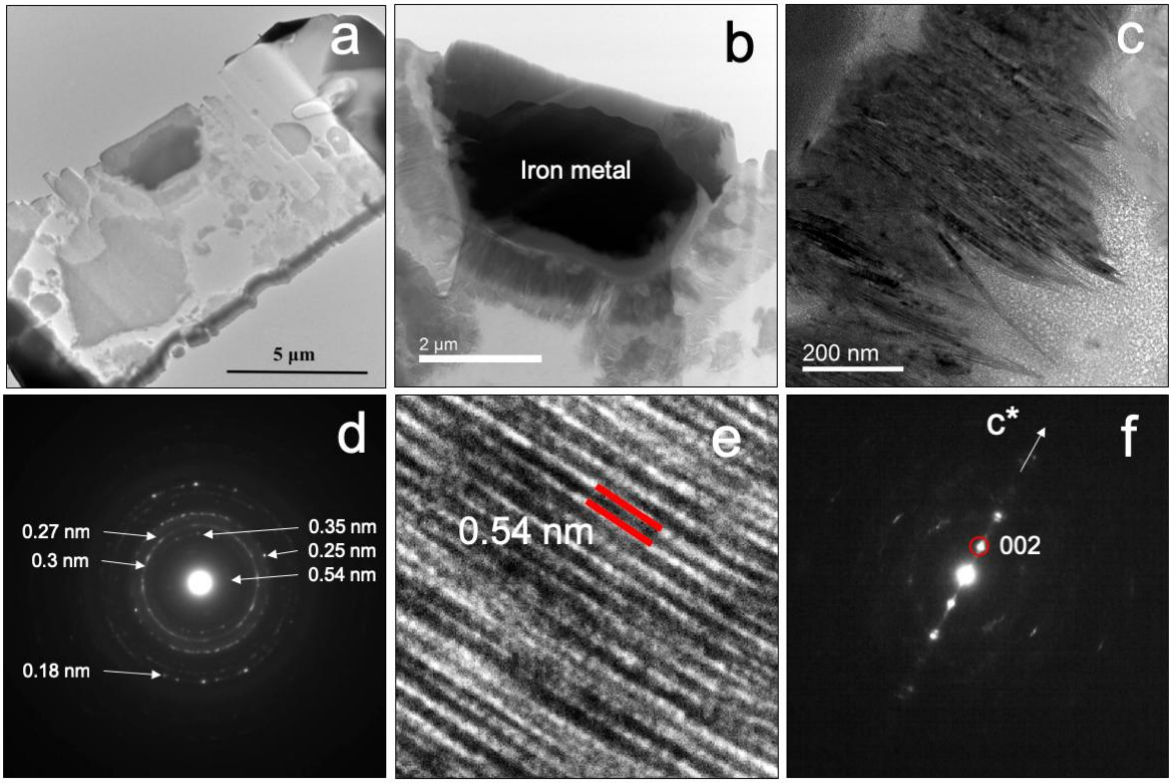
a
5 µm
b
Iron metal
2 µm
c
200 nm
d
0.27 nm
0.3 nm
0.35 nm
0.25 nm
0.54 nm
0.18 nm
e
0.54 nm
c*
f
002

Figure 8

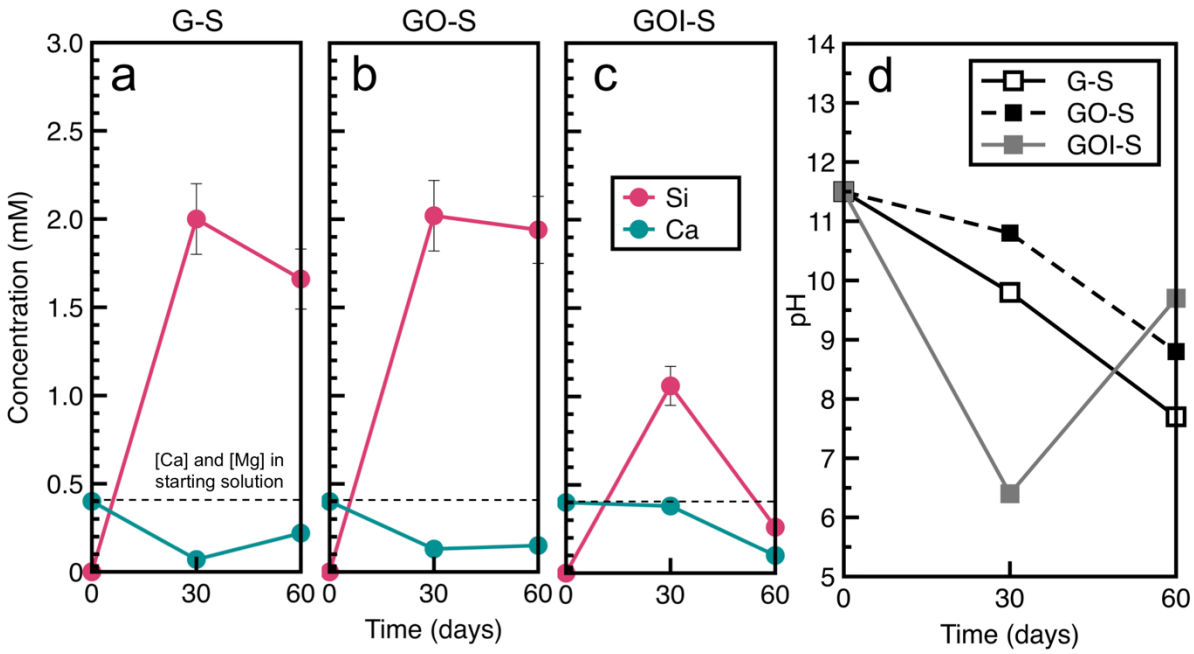

947
948 **Figure 9**
949
950

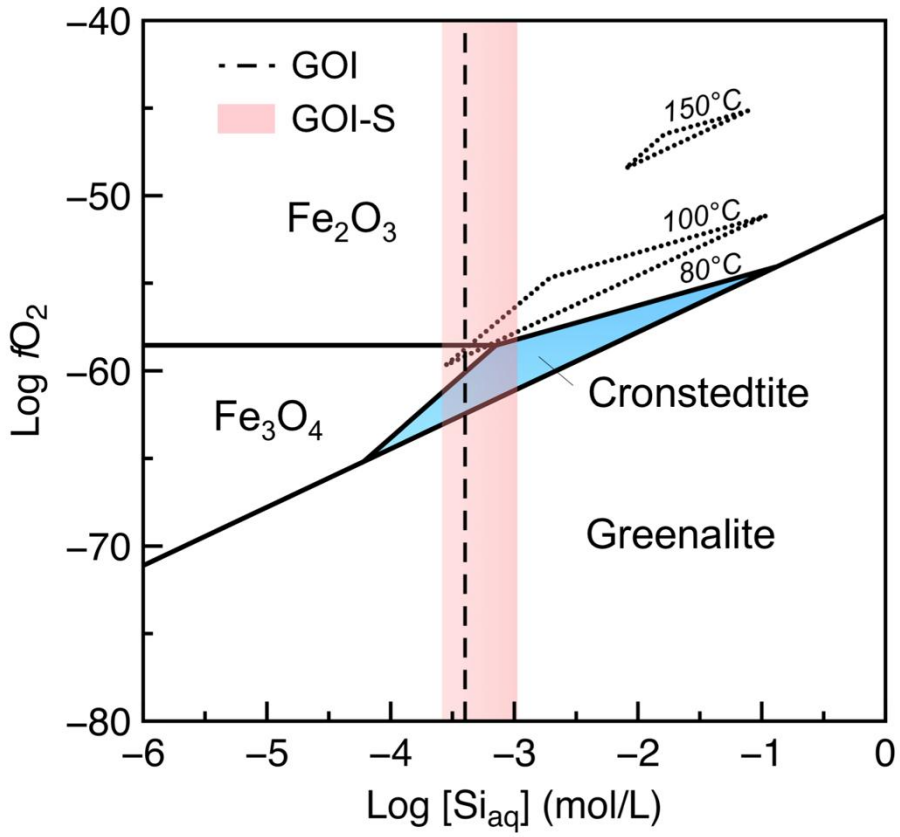

951
952 **Figure 10**
953
954

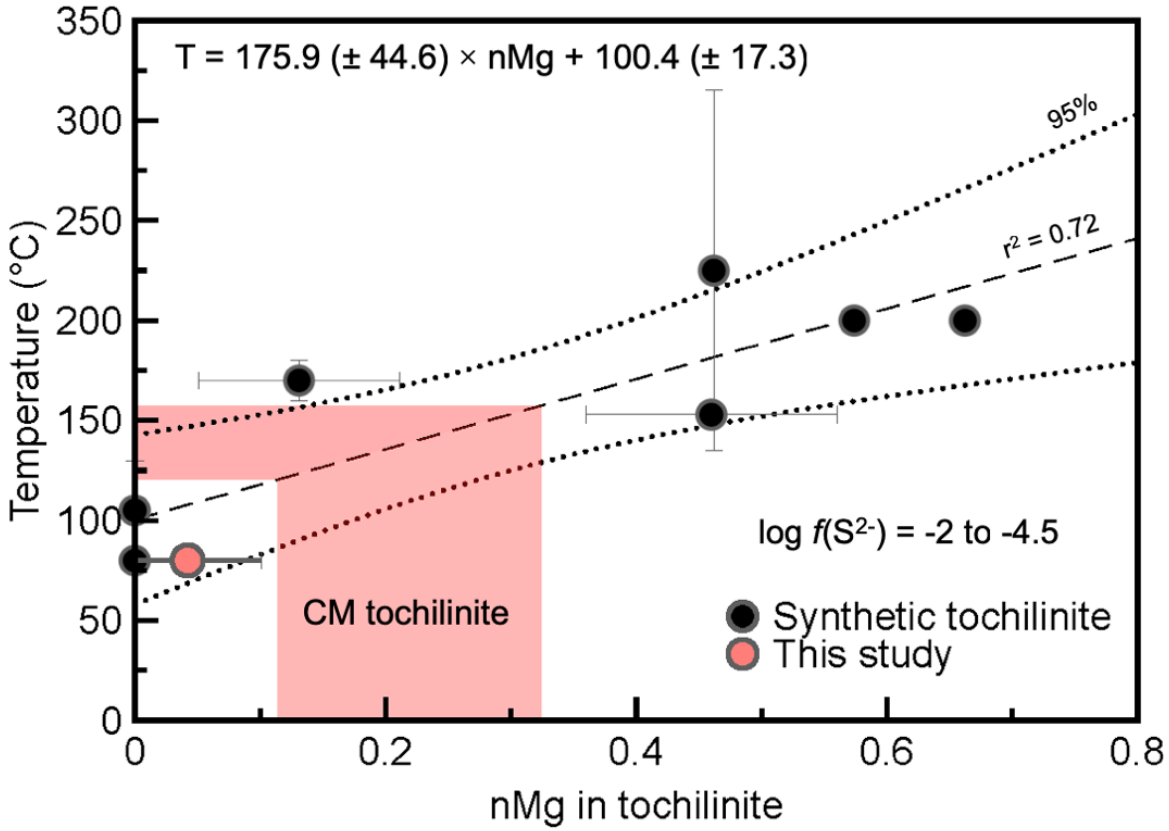
T = 175.9 (± 44.6) × nMg + 100.4 (± 17.3)
95%
r² = 0.72
log f(S²⁻) = -2 to -4.5
CM tochilinite
Synthetic tochilinite
This study
Temperature (°C)
nMg in tochilinite
0
50
100
150
200
250
300
350
0
0.2
0.4
0.6
0.8

Figure 11

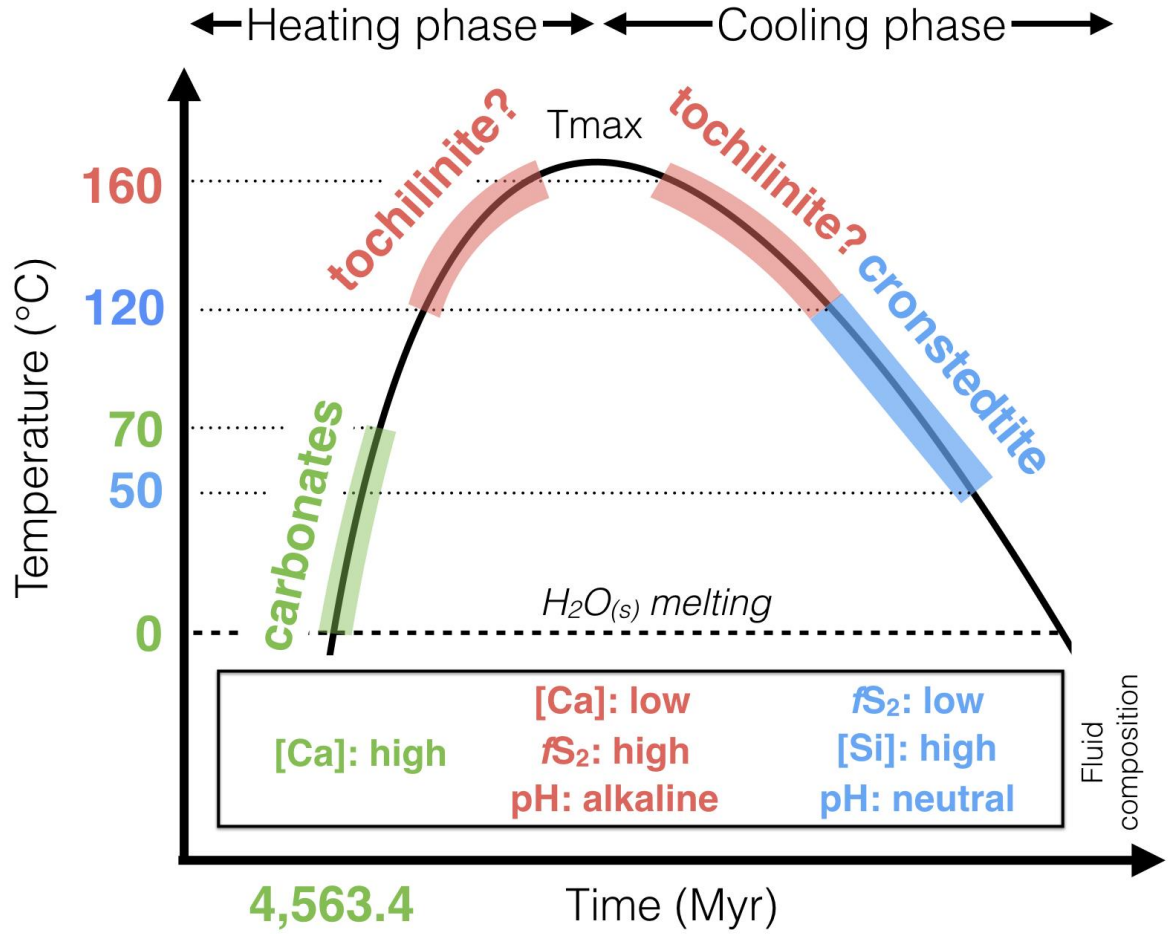
Heating phase
Cooling phase
Tmax
tochilinite?
tochilinite?
cronstedtite
carbonates
160
120
70
50
0
Temperature (°C)
$H_2O_{(s)}$ melting
[Ca]: high
[Ca]: low
fS_2: high
pH: alkaline
fS_2: low
[Si]: high
pH: neutral
Fluid composition
4,563.4
Time (Myr)

Figure 12

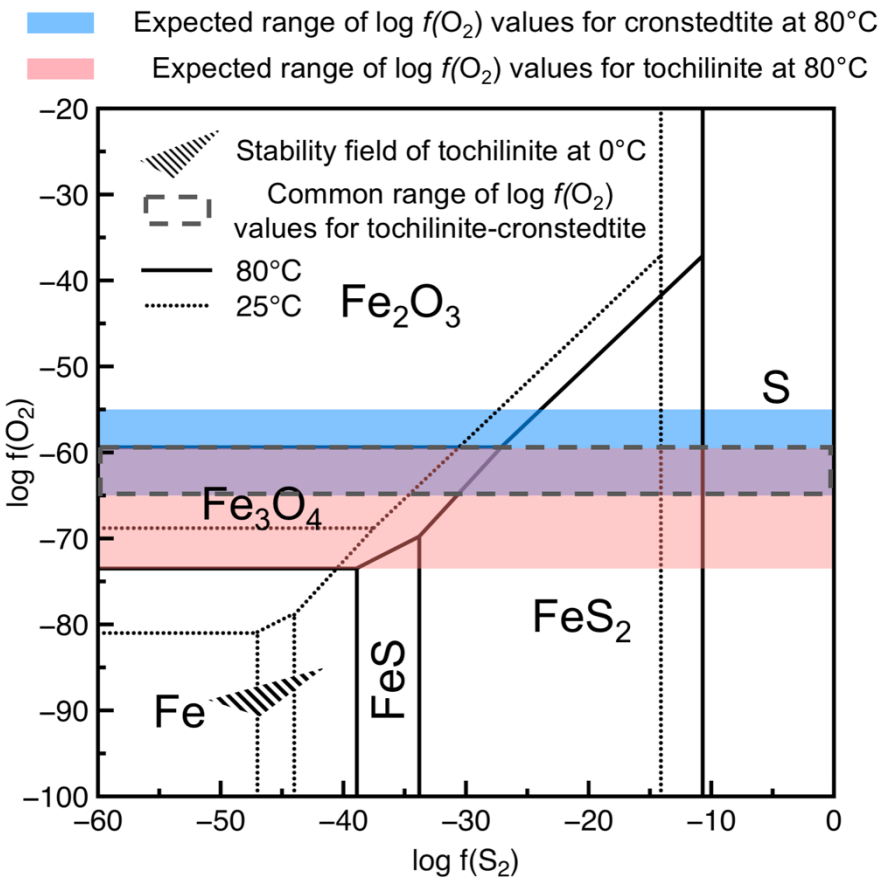

965
966

Figure 13

TABLES

Table 1. Summary of anoxic experimental conditions at 80°C and water/rock ratio = 10, and the mineral assemblages synthesized.

Table 2. Summary of hydrothermal syntheses of cronstedtite and (Fe,Mg,Al)-tochilinite.

Table 1

Run #	Synthetic GEMS-like glass (g)	Olivine (g)	Iron metal (g)	Na_2S (mM)	Time (d)	Minerals synthesized*
S-free circumneutral fluid (starting pH = 6.5 at 25°C)						
G-1	1	0	< 0.01	0	30	(Fe)-Ph + Go
G-2	1	0	< 0.01	0	60	
GO-1	0.5	0.5	< 0.01	0	30	
GO-2	0.5	0.5	< 0.01	0	60	
GOI-1	0.33	0.33	0.34	0	30	**Cr** + Go + (Fe)-Ph
GOI-2	0.33	0.33	0.34	0	60	
S-bearing alkaline fluid (starting pH = 11.5 at 25°C)						
GS-1	1	0	< 0.01	10	30	**(Fe)-To** + (Fe)-Ph + Ox
GS-2	1	0	< 0.01	10	60	
GOS-1	0.5	0.5	< 0.01	10	30	
GOS-2	0.5	0.5	< 0.01	10	60	
GOIS-1	0.33	0.33	0.34	10	30	
GOIS-2	0.33	0.33	0.34	10	60	

*(Fe)-Ph: Fe,Si-rich phyllosilicate; Mt: magnetite; Cr: cronstedtite; (Fe)-To: Fe-rich tochilinite; Go: goethite; Ox: iron oxide.

Table 2

Mineral	Time (days)	Temp. (°C)	pH	Starting material	Authors
Cronstedtite	5-120 45	80	Neutral-alkaline	Smectite + iron metal	Lantenois et al. 2005 Lanson et al. 2012
Cronstedtite	180-365	40-90	Neutral	Claystone + iron metal	Pignatelli et al. 2013, 2014
"Meteoritic" cronstedtite	20-110	110-160	Alkaline	(Fe, Mg, Al)-metal particle precursor mixture	Peng and Jing 2014
Tochilinite	2	200	Neutral-alkaline	(Mg,Al)-hydroxide gel + iron chloride (II)	Kakos et al. 1993
Fe-Tochilinite	10-150	80	Neutral-alkaline	Iron chloride (II)	Kozerenko et al. 1996
Fe-Tochilinite Mg-Tochilinite	30-150	80-360	Alkaline	Iron chloride (II)	Kozerenko et al. 2001
Tochilinite	?	160-180	Medium-alkaline	Same as Kozerenko et al. 1996	Chistyakova et al. 2006 Gubaidulina et al. 2007
(Fe, Mg)-Tochilinite	10-45	120-140	Alkaline	$Fe(OH)_2$ + metallic Mg	Moroz et al. 1997
(Fe, Mg, Al)-Tochilinite	4-60 20-110	50-120 110-160	Alkaline	(Fe, Mg, Al)-metal particle precursor mixture	Peng et al. 2007 Peng and Jing 2014
Cronstedtite Fe-Tochilinite	30-60	80	Neutral Alkaline	Glass + olivine + iron metal	This study

SUPPORTING INFORMATION

Fig. S1. BSE images of olivine grains and synthetic GEMS-like grains before and after hydrothermal experiments. a) Pristine olivine and b) synthetic GEMS-like grains before hydrothermal experiments. c) Expected unaltered olivine and d) synthetic GEMS-like grains at micrometer scale in S-free experiments after 60 days of alteration. e) Expected unaltered olivine and f) synthetic GEMS-like grains at micrometer scale in S-rich experiments after 60 days of alteration.

Table S1. Representative chemical compositions of secondary minerals formed during neutral S-free experiments (normalized to 100%); '-' indicates analyses below the detection limit.

Table S2. Dissolved cation concentrations in the run solutions equilibrated with the different synthetized products at 80°C ('-' indicates analyses below the detection limit, i.e., <50 µg/L).

Table S3. Representative chemical compositions of secondary minerals formed during alkaline S-rich experiments (normalized to 100%); '-' indicates analyses below the detection limit.

Table S4. Sulfur and Mg concentrations, Mg content in the brucite/amakinite-like layer normalized to 1 S (nMg), and precipitation temperature of synthetic and meteoritic tochilinite. Parenthetical values represent standard deviation; 'n.d.' indicates not determined.; 'n' indicates the number of values used to calculate the mean nMg value of CM tochilinites. Temperature uncertainties were calculated using the error propagation law.

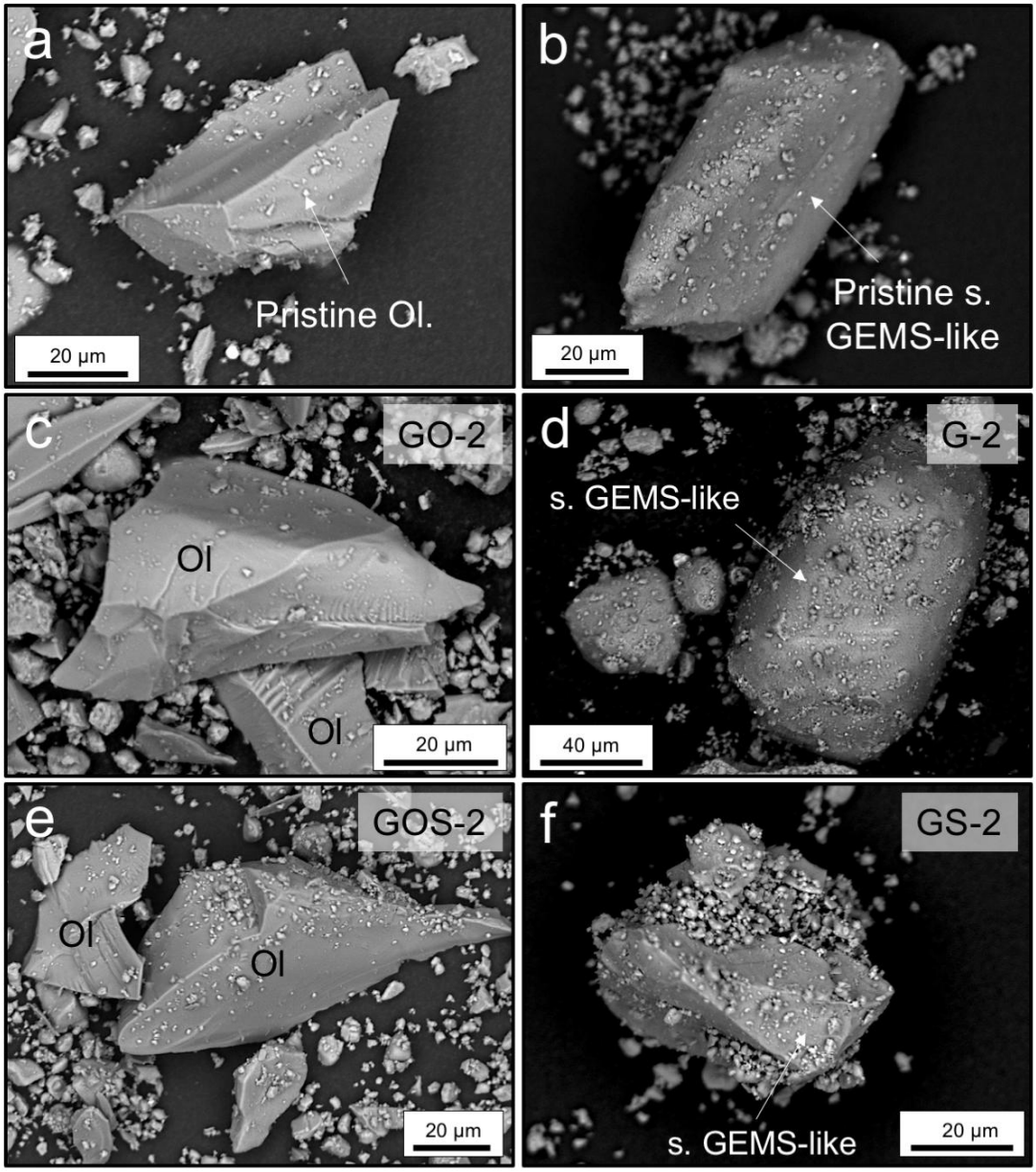
a
Pristine Ol.
20 µm
b
Pristine s.
GEMS-like
20 µm
c
GO-2
Ol
Ol
20 µm
d
G-2
s. GEMS-like
40 µm
e
GOS-2
Ol
Ol
20 µm
f
GS-2
s. GEMS-like
20 µm

Figure S1

Table S1.

Mineral phase		Si (wt.%)	Mg (wt.%)	Fe (wt.%)	Ca (wt.%)	Al (wt.%)	O (wt.%)	Total
Iron oxide	*	3.6	-	62.3	0.3	-	33.6	100
(Goethite?)	*	2.7	-	67.5	-	-	29.8	100
	*	2.7	-	68.6	-	-	28.8	100
	*	3.0	-	64.2	-	-	32.8	100
	*	3.6	-	64.3	-	-	32.0	100
	*	3.3	-	66.8	-	-	29.8	100
	*	2.9	-	66.6	-	-	30.5	100
	*	2.9	-	66.2	-	-	30.9	100
	*	4.5	1.1	62.4	-	-	32.1	100
	*	3.1	-	66.4	-	-	30.5	100
	*	3.5	-	64.4	-	-	31.7	100
Mean		**3.2**	**0.1**	**65.4**	**0.03**	**-**	**31.1**	
StDev		*0.5*	*0.3*	*2.0*	*0.1*	-	*1.5*	
Fibrous Fe,Si-rich	&	18.1	3.7	30.9	0.9	6.3	40.1	100
	&	15.6	1.9	36.9	1.6	3.9	40.2	100
Mean		**16.9**	**2.8**	**33.9**	**1.3**	**5.1**	**40.2**	
StDev		*1.8*	*1.3*	*4.2*	*0.5*	*1.7*	*0.1*	
Cronstedtite	&	8.6	0.6	53.3	0.2	1.7	35.5	100
	&	8.6	0.5	49.6	0.2	1.5	39.6	100
	&	7.9	0.4	55.5	0.1	1.4	34.7	100
	&	8.6	0.4	52.2	0.1	1.2	37.4	100
	&	7.7	0.4	53.7	0.1	1.3	36.9	100
	&	8.5	0.3	52.6	0.2	1.1	37.4	100
Mean		**8.3**	**0.4**	**52.8**	**0.2**	**1.4**	**36.9**	
StDev		*0.4*	*0.1*	*1.9*	*0.1*	*0.2*	*1.7*	

*Data from SEM-EDS analyses.

&Data from TEM-EDS analyses.

1013 **Table S2.**

Run #	Si (mM)	Mg (mM)	Fe (mM)	Ca (mM)	Al (mM)	Final pH (25 °C)
S-free, circumneutral fluid (starting pH = 6.5 at 25°C)						
G-1	0.93	0.22	43.27	0.36	0.09	6.2
G-2*	0.81	0.04	10^{-4}	0.31	4×10^{-4}	6.1
GO-1	1.22	0.44	77.89	0.31	0.13	6.1
GO-2*	0.62	0.03	7×10^{-4}	0.30	1.6×10^{-3}	7.9
GOI-1	0.40	0.28	23.10	0.22	0.04	7.2
GOI-2*	0.42	0.04	6×10^{-4}	0.24	1.5×10^{-3}	7.8
S-bearing, alkaline fluid (starting pH = 11.5 at 25°C)						
GS-1	2.00	-	-	0.07	0.01	9.8
GS-2	1.66	-	-	0.22	-	7.7
GOS-1	2.02	-	-	0.13	-	10.8
GOS-2	1.94	-	-	0.15	-	8.8
GOIS-1	1.06	0.19	-	0.38	-	6.4
GOIS-2	0.26	-	-	0.10	0.05	9.7

1014 * Because Al, Fe, and Mg concentrations are <50 µg/L, additional aliquots of solution were measured by ICP-MS with
1015 a detection limit of 1 µg/L.

1016

1017

1018 **Table S3.**

Mineral phase		Si (wt.%)	Mg (wt.%)	Fe (wt.%)	Ca (wt.%)	Al (wt.%)	O (wt.%)	S (wt.%)	Total
Fe-rich layer	*	6.6	0.0	53.3	0.5	0.4	34.0	5.2	100
	*	7.3	0.0	47.9	0.7	0.3	36.9	7.1	100
	*	7.8	0.0	43.6	1.3	0.4	39.7	7.2	100
	*	7.1	0.0	54.9	1.4	0.4	29.9	6.4	100
	*	10.3	1.0	42.1	2.4	0.9	37.5	5.7	100
	*	7.4	0.0	47.3	0.9	0.3	35.7	8.5	100
Mean		**7.7**	**0.2**	**48.2**	**1.2**	**0.5**	**35.6**	**6.7**	
StDev		*1.3*	*0.4*	*5.1*	*0.7*	*0.2*	*3.4*	*1.2*	
Fe, Si-rich layer	*	24.2	3.6	32.6	2.2	1.9	34.4	1.2	100
Mean		**23.3**	**2.7**	**33.4**	**2.0**	**1.8**	**36.2**	**0.6**	
StDev		*1.2*	*1.2*	*1.2*	*0.2*	*0.1*	*2.5*	*0.9*	
Tochilinite	*	6.5	2.1	46.5	1.2	0.9	25.4	17.4	100
	*	5.8	0.8	49.5	1.0	0.8	21.2	20.9	100
	*	4.6	0.4	52.9	1.9	0.4	23.4	16.6	100
	&	2.8	0.1	64.4	0.0	0.4	15.2	17.2	100
	&	2.5	0.0	66.9	0.0	0.6	12.6	17.3	100
	&	1.4	0.3	67.5	0.0	0.3	12.4	18.1	100
Mean		**3.9**	**0.6**	**57.9**	**0.7**	**0.6**	**18.4**	**17.9**	
StDev		*2.0*	*0.8*	*9.4*	*0.8*	*0.2*	*5.7*	*1.5*	

1019 *****Data from SEM-EDS analyses.

1020 **&**Data from TEM-EDS analyses.

1021

1022 **Table S4.**

Meteorite	S (wt.%)	Mg (wt.%)	nMg	Temperature (°C)	Authors
			Synthetic tochilinite		
	17.9 *(1.5)*	0.6 *(0.8)*	0.04 (0.06)	80	This study
	n.d.	n.d.	0	80	Kozerenko et al. 1996
	n.d.	n.d.	0	80-130	Kozerenko et al. 2001
	15.1 *(7.3)*	7.1 *(3.8)*	0.46 *(0.1)*	153	Peng and Jing 2014
	n.d.	n.d.	0.13 *(0.08)*	160-170	Chistyakova et al. 2006
	n.d.	n.d.	0.57	200	Kakos et al. 1994
	n.d.	n.d.	0.66	200	Kakos et al. 1994
	n.d.	n.d.	0.46	130-320	Kozerenko et al. 2001
			Meteoritic tochilinite (calculated temperatures)		
Paris	18.8 *(0.1)*	1.6 *(0.1)*	0.12 *(0.004)*	122 ± 38	Pignatelli et al. 2017 (n = 2)
Murchison	19 *(1.7)*	2.6 *(0.2)*	0.18 *(0.02)*	132 ± 43	Palmer and Lauretta 2011 (n = 3)
Murray	19.7 *(2.9)*	2.4 *(0.3)*	0.17 *(0.04)*	130 ± 50	Palmer and Lauretta 2011 (n = 3)
Cold Bokkeveld	19.5 *(0.7)*	4.5 *(0.2)*	0.32 *(0.004)*	157 ± 48	Palmer and Lauretta 2011 (n = 1)
Nogoya	18	4.2	0.3	153 ± 47	Palmer and Lauretta 2011 (n = 1)

1023